Atmos. Chem. Phys. Discuss., 13, 10757–10807, 2013
www.atmos-chem-phys-discuss.net/13/10757/2013/
doi:10.5194/acpd-13-10757-2013

Atmospheric Chemistry and Physics Discussions

Observation and a numerical study of gravity waves during tropical cyclone Ivan (2008)

F. Chane Ming[1], C. Ibrahim[1], S. Jolivet[2], P. Keckhut[3], Y.-A. Liou[4], and Y. Kuleshov[5,6]

[1]Université de la Réunion, Laboratoire de l'Atmosphère et des Cyclones, UMR8105, UMR CNRS-Météo France-Université, La Réunion, France
[2]Singapore Delft Water Alliance, National University of Singapore, Singapore, Singapore
[3]Laboratoire Atmosphères, Milieux, Observations Spatiales, UMR8190, Institut Pierre-Simon Laplace, Université Versailles-Saint Quentin, Guyancourt, France
[4]Center for Space and Remote Sensing Research National Central University, Chung-Li 3200, Taiwan
[5]National Climate Centre, Bureau of Meteorology, Melbourne, Australia
[6]School of Mathematical and Geospatial Sciences, Royal Melbourne Institute of Technology (RMIT) University, Melbourne, Australia

Received: 3 December 2012 – Accepted: 13 April 2013 – Published: 24 April 2013

Correspondence to: F. Chane Ming (fchane@univ-reunion.fr)

Published by Copernicus Publications on behalf of the European Geosciences Union.

ACPD
13, 10757–10807, 2013

Abstract

Activity and spectral characteristics of gravity-waves (GWs) are analyzed during tropical cyclone (TC) Ivan (2008) in the troposphere and lower stratosphere using radiosonde and GPS radio occultation data, ECMWF outputs and simulations of French numerical model Meso-NH with vertical resolution varying between 150 m near the surface and 500 m in the lower stratosphere. Conventional methods for GW analysis and signal and image processing tools provide information on a wide spectrum of GWs with horizontal wavelengths of 40–1800 km and short vertical wavelengths of 0.6–10 km respectively and periods of 20 min–2 days. MesoNH model, initialized with Aladin-Réunion analyses, produces realistic and detailed description of TC dynamics, GWs, variability of the tropospheric and stratospheric background wind and TC rainband characteristics at different stages of TC Ivan. In particular a dominant eastward propagating TC-related quasi-inertia GW is present during intensification of TC Ivan with horizontal and vertical wavelengths of 400–600 km and 1.5–3.5 km respectively during intensification. A wavenumber-1 vortex Rossby wave is identified as a source of this medium-scale mode while short-scale modes located at north-east and south-east of the TC could be attributed to strong localized convection in spiral bands resulting from wavenumber-2 vortex Rossby waves. Meso-NH simulations also reveal high-frequency GWs with horizontal wavelengths of 20–80 km near the TC eye and high-frequency GWs-related clouds behind TC Ivan. In addition, GWs produced during landfall are likely to strongly contribute to background wind in the middle and upper troposphere as well as the stratospheric quasi-biennial oscillation.

1 Introduction

Mesoscale organized convective systems such as tropical cyclones (TCs) have been known as intense sources of convectively-generated gravity waves (GWs) with horizontal wavelength of 10–2000 km, vertical wavelengths of 1–6 km and periods of 1 h–

ACPD
13, 10757–10807, 2013

2.5 days in the upper troposphere (UT) and lower stratosphere (LS) above TC basins (Pfister et al., 1993; Sato et al., 1993; Chane Ming et al., 2002, 2010; Dhaka et al., 2003; Niranjan Kumar et al., 2011; Das et al., 2012). Recently, using radiosonde data, Chane Ming et al. (2010) also demonstrated a possible correlation between daily maximum surface wind speed and total energy density of low frequency GWs produced by intense TCs Dina and Faxai in the UT/LS. Ibrahim et al. (2010) extended this study analysing a climatology of 10 TC seasons (1997/1998–2006/2007) and radiosonde data obtained at Tromelin Island (15.53° S, 54.31° E) located in the south-west Indian ocean (SWIO). Results suggest a possible linear relationship between weekly GW total energy density in the LS and cyclone-days of intense TCs in the SWIO.

Non-orographic GWs triggered by deep convection play an important role in tropical dynamics (Piani et al., 2000; Lane and Reeder, 2001), in particular in the quasi-biennal oscillation (Baldwin et al., 2001) and the mesopause semi-annual oscillation (Dunkerton, 1982) in the equatorial region. As various source mechanisms of such intermittent small-scale waves are not clearly understood, observations as well as high-resolution mesoscale numerical modelling are needed to improve parameterizations of such unresolved processes in weather forecasting and climate models (Kim et al., 2003; Alexander et al., 2010). In addition, GW drag parameterizations fail to represent correctly non-orographic GWs produced by convection in general circulation models because of a wide spectrum of phase speeds, wave frequencies and spatial scales depending on properties of convection and the environment (Richter et al., 2010). Thus GW drag parameterizations require a set of observations of source properties covering a good spectral range to constrain tunable parameters for realistic global behavior of both orographic and non-orographic GWs through GW momentum fluxes (Alexander, 2003; Fritts and Alexander, 2003). Therefore implementation of GW momentum flux parameterizations dedicated to specific convective source processes in Global Climate Models (GCMs) is a current research topic (Ern and Preusse, 2012). For example, Kim and Chun (2005) suggested a computationally efficient non-orographic GW parameterization scheme producing reasonably accurate variation of the momentum flux

ACPD
13, 10757–10807, 2013

generated by convective heat sources for global atmospheric prediction models in the middle atmosphere.

Presently, prediction of TC intensity and its change is limited by our understanding of TC structure and multi-scale interaction inside and with the environment. Wave processes, especially in the inner core dynamics, and their relationship with spiral rainbands are not fully understood. In particular, sources of GWs and effects on TC structure still remains an open debate (Chow and Chan, 2003; Schubert et al., 2007; Schecter, 2008; Hendricks et al., 2008). Indeed current sophisticated mesoscale numerical models showed evidence of GWs in the inner core and rainbands in high resolution simulations (Liu et al., 1999; Zhang et al., 2000, 2002; Lin et al., 2011). In resolving explicitly convection, mesoscale models such as MM5 (Fifth-Generation NCAR/Penn State Mesoscale Model PSU/NCAR Mesoscale Model) and AR-WRF (Advanced Rechearch-Weather Research and Forecasting) are useful numerical tools to explore GWs frequently observed during TCs such as source mechanisms, propagation and effects on the atmosphere in relation with evolution of the TC dynamics (Kim et al., 2005; Kuester et al., 2008). Simulation of TC Saomai (2006) suggested a possible impact of TC-related GWs on the TC development through the modification of the tropospheric vertical wind shear (Kim and Chun, 2011).

In this study, GWs are examined during the evolution of TC Ivan (2008) in the SWIO using French mesoscale model Méso-NH. Characteristics of GWs are derived at different stages of the cyclone's development prior to and after landfall using model simulations and observations. Radiosonde data are obtained from meteorological stations (Gillot and Ivato), GPS radio occultation (RO) data from FORMOSAT-3/COSMIC, and meteorological analyses from ECMWF. Characteristics of TC rainbands are also investigated.

ACPD
13, 10757–10807, 2013

2 Overview of tropical cyclone Ivan (2008)

Developing from a disturbed area of convection with a sustained monsoon flux in the lower layers, the system became well-organized northeast of Madagascar on 6 February 2008. Due to a rapid intensification favoured by the passage of a tropopause anomaly above, it reached a stage of moderate tropical storm on 7 February. Moving south-eastward, the system oscillated between stages of moderate tropical storm and strong tropical storm on 11 and 12 February. It reversed course from 9 to 12 February, making a complete loop and turning to the west-south-west after 14 February. Encountering new favourable conditions after 14 February, the system re-intensified to a TC stage as it passed over Tromelin Island on 15 February. Then TC Ivan continued moving towards the west-southwest at an average speed of 8 knots, becoming a threat to the northeast coast of Madagascar. TRMM PR captured tall convective activity with high values of reflectivity (30 dBz) at 10–11 km heights on 16 February at 06:21 UTC. Tall towers, elevated up to about 13 km height, were observed in the concentric inner eyewall and in TC spiral rainbands at the beginning of its intensification. Figure 1a shows satellite observation of TC Ivan at the beginning of the intense stage of development on 16 February at 00:00 UTC. Minimum central pressure of 920 hPa and 10 min averaged maximum sustained winds of 105 knots were reported on 16 February at 06:00 UTC (Fig. 1b). Figures 1c and d show evidence of a wavenumber-1 asymmetry characterized by an increase (a decrease) of convection close to the eyewall in the north-eastern (south-western) quadrant of the TC on 16 February at 16:30 UTC and 17 February at 00:00 UTC respectively. Eyewall asymmetries are common feature for TCs and are now considered to be crucial for understanding internal dynamics and variability of TC intensity (Hendricks et al., 2012). Using airborne Doppler radar, Marks et al. (1992) investigated the nature of the altitude-varying wind asymmetry of TC Norbert (1984). The asymmetry perturbations were characterized as a source-sink field at 1 km heights and a vortex couplet above 3 km heights (Marks et al., 1992; Liu et al.,

ACPD
13, 10757–10807, 2013

1999). Indeed, most of this asymmetry of TC Olivia (1994) could be explained by the azimuthal variance of wavenumber-1 above 3 km height (Reasor et al., 2000).

On 17 February at 04:00 UTC, TC Ivan passed over Sainte Marie Island and then it made a landfall in the north of Madagascar at 06:00 UTC with maximum sustained winds of 95 knots and a minimum central pressure of 935 hPa (Fig. 1d). It rapidly weakened into a remnant low pressure area as it crossed Madagascar. It regenerated over the Mozambique Channel into a tropical depression from 19 February before dissipation on 22 February. Best track data of TC Ivan from 13 February until its landfall in Madagascar are presented in Fig. 2.

3 Data and methodology

Characteristics of GWs are derived using upper air data obtained by GPS radiosondes launched at meteorological stations of Gillot (20° 53′ S, 55° 30′ E) at La Reunion Island and Ivato (18° 53′ S, 47° 48′ E) at Antananarivo in Madagascar, FORMOSAT-3/COSMIC GPS RO dataset within the area encompassed by longitudes between 48° E and 68° E and latitudes between 10° S and 22° S, and ECMWF analyses during TC Ivan in February 2008 (Fig. 2). From 5 February to 27 February, 23 GPS radiosondes were launched daily at 11:00 UTC at the airport of Gillot (21 m altitude). Vertical profiles of temperature and horizontal wind with 100 m resolution reached the mean altitude of 23 km. Radiosonde data quality and accuracy are described in Chane Ming et al. (2002, 2007, 2010) and Ibrahim (2010) which used similar vertical profiles to characterize GWs in the UT/LS. At Ivato airport (389 m altitude), 40 GPS radiosonde profiles were obtained twice a day at 00:00 and/or 09:00 and/or 12:00 UTC with a vertical resolution of 300 m and a mean maximum altitude of 23 km.

The FORMOSAT-3/COSMIC (Formosa Satellite Mission-3/Constellation Observing System for Meteorology, Ionosphere, and Climate) dataset from the COSMIC Data Analysis and Archive Center (CDAAC) consists of 70 daily soundings of temperature between 2 and 40 km altitude over the SWIO between 13 and 18 February 2008. Ver-

ACPD
13, 10757–10807, 2013

tical profiles have high accuracy for temperature (<1 K from 5 km to 25 km) and spatial resolution varying from 100 m at the surface to 1.5 km at 35 km altitude (1 km at the tropopause) (Pirscher et al., 2010; Anthes, 2011). Collocation mismatch affects the comparison: standard deviation errors are < 0.5 K for temperature in both the troposphere (850–200 hPa) and stratosphere, and for relative humidity are < 3.5 % for 3 h temporal buffer and 100 km spatial buffer (Sun et al., 2010; Zhang et al., 2011). GPS RO data observed by low-earth-orbit satellites have been used previously for GWs observations in the LS (Liou et al., 2003, 2006). A comprehensive introduction to the RO method for remote sensing of the atmosphere and ionosphere is presented by Liou et al. (2010). COSMIC GPS RO profiles recently have been analyzed to describe monthly global stratospheric GW energy densities (Alexander et al., 2008; Xiao and Hu, 2010).

In the present study, vertical velocities are extracted from 6 hourly ECMWF ERA-40 operational analyses of T150 1.125° × 1.125° spectral resolution for the analysis of GWs in the UT/LS. Mountain and jet-stream-forced GWs have been previously derived from ECMWF data (Plougonven and Teitelbaum, 2003; Schroeder et al., 2009). Indeed current operational numerical weather prediction models (NWPs) are likely to resolve explicitly a large fraction of the observed stratospheric inertia-gravity wave spectrum with horizontal wavelengths of 100–1000 km and probably even longer in the tropics (Shutts and Vosper, 2011). Nevertheless, vertical resolution still remains insufficient to capture quasi-inertia wave energy with vertical wavelengths less than 2 km. In addition, high-quality temperature information in ECMWF data are provided in the UT/LS, more particularly in the Southern Hemisphere, ever since the assimilation of GPS RO bending angles beginning in late December 2006 (Healy and Thepaut, 2006; Healy, 2007). Thus several studies proved that TC simulations are also improved in NWP models (Huang et al., 2010; Kunii et al., 2012; Liu et al., 2012).

Second- and third-order polynomial fits are applied to GPS radiosonde vertical profiles of temperature and wind respectively, using a cubic spline interpolation, and subtracted from the 100-m resampled vertical profiles to derive temperature and

ACPD
13, 10757–10807, 2013

wind perturbations induced by GWs. Conventional methods mentioned in Chane-Ming et al. (2010) are applied to vertical profiles of temperature and wind perturbations to extract GW parameters such as energy densities and spectral characteristics. One- and two-dimensional Fast Fourier Transforms (FFT) and Morlet wavelet techniques together with other image processing tools are used to visualize and to extract spectral characteristics of GW signature embedded in GPS RO vertical perturbation profiles, ECMWF analyses and Meso-NH outputs respectively. Second-order spectral parameters are derived from the linear relation of GW dispersion.

4 Numerical experiment

4.1 Model description

The non-hydrostatic Mesoscale model Meso-NH (Lafore et al., 1998) is used in this study to simulate development of TC Ivan from 13 to 18 February. The model has been jointly developed by the Centre National de Recherches Météorologiques (Centre National de la Recherche Scientifique/Météo-France) and Laboratoire d'Aérologie (Centre National de la Recherche Scientifique/Université Paul Sabatier). In previous studies, the model proved to be useful for simulation of cyclone development. Nuissier et al. (2006) studied a mature stage of category 4 TC Bret (1999) in the North Atlantic basin with the Meso-NH non-hydrostatic, two-way interactive, quadruple-nested grid mesoscale model initialized with airborne Doppler radar and dropsonde data. Leclaire De Bellevue et al. (2007) focused on tropospheric ozone enhancement at the periphery of TC Marlene in the SWIO. Recently orographic influence of La Réunion Island on the structure and evolution of TC Dina (2002), described in Roux et al. (2004), was numerically examined in Jolivet et al. (2013). Particularly, PV estimates revealed that buoyancy waves were generated on the lee side of the island's peak, when peripheral cyclonic flow of the TC hits the island.

ACPD
13, 10757–10807, 2013

The present model configuration consists of a single domain with 360×600 horizontal grid points (4 km resolution) in order to study GWs with horizontal wavelengths between 32 km ($8\Delta x$) (Lane and Knievel, 2005) and 1200–1600 km. Fifty-five vertical levels are used from the surface to 29 km altitude with a damping layer at 25 km. The vertical resolution decreases with altitude from about 150 m in a zone of low-level convergence to about 500 m in the UT/LS. The simulation started at 00:00 UTC on 13 February 2008 (time step of 15 s), when TC Ivan begun moving to the southwest in the direction of Tromelin and Madagascar and ended at 21:00 UTC on 18 February 2008 after its landfall in Madagascar. Thus, the intensification, mature stage and dissipation of TC Ivan are reproduced in the numerical model.

Meso-NH is initialized and forced at boundaries by Aladin-Réunion 6 h analyses. Aladin-Réunion is a limited area model used by Météo-France for TC forecasting in the SWIO since 2006 (Montroty et al., 2008). It better represents TC structure in comparison with global models so that no bogus is used in this model. Physics of the model includes a mixed-phase microphysics scheme (Pinty and Jabouille, 1998), and a 1-D turbulence scheme (Cuxart et al., 2000). Shallow convection is parameterized with the scheme of Kain and Fritsch (1990) adapted by Bechtold et al. (2001). The same scheme is used for simulation of deep convection to the resolution of 5 km. At this resolution and below, deep convection is explicitly resolved by the model. The radiative scheme is the one used at ECMWF (Gregory et al., 2000).

4.2 Validation of simulated TC Ivan track

A simulated track is compared with best track data prepared by Météo-France Regional Specialized Meteorological Centre (RSMC) La Réunion (Fig. 2). TC categories used for classification of TC intensity by the RSMC La Reunion are based on 10 min average maximum sustained winds. After a 24 h spin-up, a track of TC Ivan is well represented in the model. At the beginning of the simulation, the system moved to the northwest before heading toward Madagascar. This simulated track becomes more consistent with the observed track from the TC intensification stage to its landfall in Madagascar.

ACPD
13, 10757–10807, 2013

A position error of less than 50 km is observed during the intense phase of TC Ivan (from 16 February at 00:00 UTC to 17 February at 21:00 UTC) compared with best track data. A simulated landfall on Sainte Marie Island occurred with a delay of 3 h. A TC tracker algorithm is based on detecting minimum pressure with a location uncertainty of about 10 km. Evolution of the maximum sustained windspeed and minimum central pressure is illustrated in Fig. 3. The simulated parameters are in good agreement with the observations after the spin-up phase. In the model simulation, the TC intensity is slightly underestimated during the cyclone's mature stage. The minimum central pressure (maximum sustained winds speed) decreases (increases) to a minimum (maximum) of 940 hPa (53 m s^{-1}) until 16 February.

Synthetic brightness temperatures corresponding to the Meteosat Second Generation (MSG) observations in the infrared channels were computed from MesoNH outputs using the Radiative Transfer for Tiros Operational Vertical Sounder (RTTOV) code version 8.7 (Saunders et al., 2005), and compared with observations (Chaboureau et al., 2000). Brightness temperatures observed with Meteosat-7 and computed from Meso-NH outputs on 16 February 2008 at 00:00 UTC for the intense stage of TC Ivan are presented in Fig. 4. Meso-NH reproduces a TC eye characterized by a zone of high brightness temperature in the centre of TC Ivan (218 K for Meteosat-7 and 214 K for Meso-NH). An asymmetry of the system is well represented with an area of more intense convection in the northeastern quadrant characterized by low values of brightness temperature (192 K and 190 K for observations and Meso-NH, respectively). This area is more extended for the Meso-NH simulation at this time.

Simulated temperature and wind fields on 15 and 16 February at 00:00 UTC in the outer region of the storm are also examined. Both radiosonde and GPS RO vertical profiles of temperature are quite consistent with simulated fields of the environment in the troposphere at altitudes between 1 km and 25 km with relative mean errors < 1.5 % at distance of 650 and 825 km from the centre of TC Ivan, respectively (Fig. 5a). A general behavior of temperatures is correctly simulated in the outer region of the storm in the troposphere (Fig. 5a, b). Differences observed in mean temperature above 20 km

ACPD
13, 10757–10807, 2013

at distance of 650 km do not affect GWs on profiles of temperature perturbations below 20 km altitudes (Fig. 5a). In addition, variations of mean simulated horizontal winds (Fig. 5c, d) are observed to be in good agreement with observed wind fields (mean relative error of about 5 %) at altitudes between 5 km and 25 km. Vertical behavior of mean horizontal wind affects vertical propagation of GWs in the UT/LS through critical level filtering.

Consequently, the track, intensity and structure as well as the outer environment of TC Ivan are well-simulated by Meso-NH for a realistic study of GWs.

5 Characteristics of GWs

5.1 Radiosonde and GPS RO data

Spectral characteristics of GWs are first derived in the UT (10–15 km) and LS (18–22 km) from the radiosonde dataset using conventional methods during TC stage of Ivan from 15 to 18 February (Table 1). The altitude range of radiosonde data in the LS above Ivato limits the study to the UT. Periods of GWs are observed to be shorter in the UT (7.4 h and 4.6 h) than in the LS (13 h). GWs have vertical wavelengths between 0.68 and 2.6 km and horizontal wavelengths of 84 and 210 km in the UT. Rotary spectral analyses provide a dominant eastward horizontal direction of GW propagation (40°–70° from North) in the UT and LS from 16 to 18 February above Gillot. Horizontal phase speeds of 3.58 $m\,s^{-1}$ and 10.75 $m\,s^{-1}$ are estimated for horizontal wavelengths of 130 and 390 km respectively in the LS from 16 to 18 February. A maximum upward energy of 70 % in both the UT and the LS and critical level filtering effects associated with zonal winds varying continuously between 10 $m\,s^{-1}$ at 11 km and −25 $m\,s^{-1}$ at 25 km (Fig. 5c and d) suggest that GW sources are located below 11 km. On the other hand, a maximum upward energy of 58–70 % is observed in the UT during landfall after the passage of the TC above Ivato. Thus, different processes might be involved in

ACPD
13, 10757–10807, 2013

the generation of GWs above the two meteorological stations before and after landfall (Chane Ming et al., 2002, 2010).

Daily dominant vertical wavelengths are computed from 70 profiles of GPS RO data from 13 to 18 February in the UT (10–15 km) and the LS (18–24 km). A dominant vertical wavelength of 3 km is observed during the whole period in the UT and LS above the SWIO basin, especially behind TC Ivan (Fig. 6). In the LS, energy intensity of the 3-km vertical mode is larger from the intensification to landfall of TC Ivan (from 15 to 18 February) and maximal during the intense stage of TC Ivan on 16 February. The opposite is observed in the UT. It is consistent with climatological observations of GW activity during TC seasons (Ibrahim et al., 2010). In contrast, peaks of GW energy densities during very intense TCs were observed both in the UT and the LS (Chane Ming et al., 2010; Ibrahim et al., 2010).

Vertical wavelengths of collocated profiles of GPS RO temperature fluctuations and radiosonde data (distance < 100 km and time < 3 h) on 15 and 16 February at Gillot and Ivato are examined. A dominant mode of 3-km vertical wavelength is observed in radiosonde and GPS RO profiles in the UT/LS on 15 February above Gillot (Fig. 7). Better vertical resolution of radiosonde data enables observation of smaller vertical wavelengths of 800 m and 590 m in the LS. Similar dominant modes with vertical wavelengths of 650 m and 3.1 km in the UT and 1.6 km in the LS are present on FFT spectra during the TC stage of the system because of radiosonde and GPS RO soundings at Ivato have the same vertical resolutions in the UT. GWs have a broader spectrum of vertical wavelengths > 1 km above Ivato located in an orographic region. In addition, FFT energy is more intense both in the UT and the LS above Gillot in contrast to that above Ivato located ahead of TC Ivan, especially in the UT. The observational filter of GPS RO measurements preferentially observes GWs with periods > 2 h (Preusse et al., 2008).

In conclusion, radiosonde and GPS RO temperature profiles show evidence of consistent observations of low-frequency GW dominant modes with vertical wavelengths of 0.6–1 km and 2.1–3 km above Gillot in the UT/LS and above Ivato in the UT during

ACPD
13, 10757–10807, 2013

the TC stage of Ivan. In contrast, a dominant mode with vertical wavelength of 1.6 km is detected on 16 and 17 February in the LS above Ivato. Low-frequency GWs with periods of 4–8 h are observed in the UT while quasi-inertia GWs with period of 13 h are present in the LS above Gillot.

5.2 ECMWF analyses

A spatial high-pass bi-directional 2-D-filter is applied on vertical velocity derived from ECMWF analyses to enhance horizontal and vertical gradients. Filtered vertical velocity shows evidence of semi-circular waves with a dominant horizontal wavelength of about 600 km behind TC Ivan dissipating within a distance as far as four times the horizontal wavelength (2500 km) at 21 km altitude in the LS on 16 February 2008 (Fig. 8a). The centre of concentric patterns is located in the northwestern side at a distance of 350 km from the TC centre (16.5° S, 53° E). In Fig. 8b, a spectral analysis of vertical velocity at latitudes of the TC centre (16.5° S) and observed GWs (9–21° S) also reveals presence of other wavelike structures with horizontal wavelengths of 460 km, 860 km, 1100 km and 1700 km, for which spectral peaks are maximum at latitudes close to TC centre. The horizontal wavelength-latitude diagram clearly indicates that most of energy distribution is located at latitudes between 7° S and 21° S (Fig. 8c). A line of symmetry is at latitudes of about 14–16° S. Waves with long horizontal wavelengths of 1400–1700 km are confined to latitudes of 15–16.5° S where as those with horizontal wavelengths of about 600 km are dominant at a distance of about 300 km from the TC eye. More intense and concentric similar patterns in the UT at 13-km altitude during the intensification of TC Ivan are indicative of background wind filtering above 13 km (Fig. 5c) for westward propagating modes with horizontal wavelengths of about 600 km and the location of GW sources in the UT. Thus the one-dimensional FFT spectra indicate that T150 ECMWF analyses reveals presence of wavelike structures with vertical wavelengths > 1000 km and fail to capture those with horizontal wavelengths < 350 km during the evolution of TC Ivan in contrast with GPS RO and radiosonde profiles, owing to the horizontal resolution of ECMWF analyses. Morlet continuous wavelet transform

ACPD
13, 10757–10807, 2013

(CWT) is applied to the vertical velocity at the latitude of the TC eye to derive location of observed horizontal modes (Chane-Ming et al., 1999). Longitude-horizontal wavelength distribution derived from CWT modulus shows evidence of a dominant mode of about 550 km of which maximum intensity is at latitude of 61° S behind TC Ivan (Fig. 8d). A large continuous spectrum of GWs with horizontal wavelengths between 350 km and 1000 km is observed behind the TC eye while a dominant mode of about 800 km horizontal wavelength is present ahead of the TC eye with little horizontal extension. In addition CWT diagram reveals the possible presence of a longer mode with 1700 km horizontal wavelength ahead of TC Ivan.

The observed phase relationships between perturbation zonal, meridional, and vertical winds and temperature at latitude of 16.5° S agrees with linear gravity wave theory for the dominant observed GWs (Gill, 1982). The ratio between CWT modulus of horizontal wind perturbations is computed for the continuous spectrum of GWs with horizontal wavelengths between 350 km and 1000 km to determine the intrinsic period from Eq. (1) in Chane Ming et al. (2002). Mean periods of 14 h and 12.8 h are obtained for the whole area and behind TC eye respectively. The ratio between CWT modulus of zonal and vertical wind perturbations provides vertical wavelengths of 1–2 km for the dominant mode of 600 km horizontal wavelength and 12.8 h period. Mean horizontal and vertical observed phase speeds are estimated of about $13\,m\,s^{-1}$ and $-0.04\,m\,s^{-1}$ respectively. A mean period of 1–1.8 days is obtained for GWs with horizontal wavelengths between 1400 km and 1700 km with a dispersive vertical wavelength > 4 km peaking between 5–10 km. Such periods correspond to inertial periods for latitudes between 5° S and 15° S. Mean horizontal and vertical phase speeds vary between $10\,m\,s^{-1}$ and $20\,m\,s^{-1}$ and between -0.03 and $-0.08\,m\,s^{-1}$ respectively.

Both FFT and CWT transforms also support that winds have a directional filtering effect on propagation of TC-induced GWs from the UT to the LS.

Thus, observations are consistent with previous studies on GWs triggered by convective turrets (Dewan et al., 1998; Piani et al., 2000; Lane and Reeder, 2001; Horinouchi et al., 2002). ECMWF analyses reveal that convection related to TC Ivan is a source

ACPD
13, 10757–10807, 2013

of a large spectrum of GWs in the UT. In particular a dominant mode of horizontal and vertical wavelengths of 600 and 1–2 km respectively and 12.8 h period is observed east of the TC with an eastward propagation of about 13 $m s^{-1}$ favored by the westward background wind in the UT and LS. Finally the study also reveals that ECMWF model is able to capture GWs with horizontal wavelengths > 350 km, vertical wavelengths < 2 km and some inertia-GWs (Shutts and Vosper, 2011).

5.3 Simulated GWs

Vertical profiles of meridional wind perturbations are extracted from the simulation every 10 min to examine small-scale vertical wave activity from 13 February at 00:00 UTC to 18 February at 12:00 UTC above Tromelin Island which is located on the track of TC Ivan (Fig. 9a). A third-order polynomial fit is used to derive vertical profiles of perturbations. Wave activity with a vertical wavelength of about 2.3 km is clearly observed in the LS up to 25 km altitude during the development stage of TC Ivan from 14 to 15 February. The downward phase progression estimated at about $-0.08 m s^{-1}$ reveals an upward energy propagation of convective GWs. GW activity increases in the UT at altitudes between 13 and 15 km and in the lowermost stratosphere after the passage of TC Ivan over Tromelin Island during the intensification stage from 16 February with a downward phase progression between −0.02 and $-0.06 m s^{-1}$. It weakens during the mature stage and increases in the UT again during landfall on 17 February. This suggests that sources of such waves are located above TC Ivan at altitudes between 13 and 15 km. Wavelike structures with longer vertical wavelengths of about 4 km and a clear upward phase progression ($0.06 m s^{-1}$) are also visualized in the middle troposphere at altitudes of 5–10 km on late 16 February during the mature stage of the TC. They are more intense in the afternoon of 17 February during landfall of TC Ivan and on 18 February. Large GW energy density was observed previously in the UT/LS during intensification of TC Dina (Chane Ming et al., 2010) and landfalls of TC Hudah (2000) over Madagascar and Mozambique (Chane Ming et al., 2002). Time series of simulated vertical flux of horizontal GW momentum at Tromelin and La Réunion islands

ACPD
13, 10757–10807, 2013

indicate that the major peak in the LS is associated with the rapid intensification of TC Ivan.

Time series of simulated vertical profiles of mean zonal wind at Gillot display strong westward winds above the surface from 16 February until TC landfall (Fig. 9b). They are accompanied with stronger eastward zonal wind below the tropopause during TC intensification and landfall where strong GW activity occurs.

Westward wind at 4 km altitude increases during intensification. Strong westward winds are also visualized above 25 km in the LS during TC intensification and at 23–25 km altitudes during landfall. Eastward zonal wind, appearing initially in a shallow layer in the UT, increases in strength during cyclone passage to the north, then deepens into the middle troposphere after landfall. Figure 9c shows zonal winds at 300 km off the TC centre increasing from 0 m^{-1} to about $-25\,m\,s^{-1}$ and meridional winds varying between $-5\,m\,s^{-1}$ and $5\,m\,s^{-1}$ at altitudes between 16–25 km on 16 February at 06:00 UTC. In addition eastward winds are observed east of the TC centre in the UT. Thus increase of eastward zonal wind in the middle troposphere and UT suggests that some eastward GWs are absorbed by the background wind.

Indeed, time series of vertical profiles of zonal wind at Mahe (4.66° S, 55.53° E) show the downward propagation of westward QBO winds (0.8 km/month) from January to late May 2008 located between 20–22 km altitudes during TC Ivan and the occurrence of eastward QBO winds above 22 km altitude in agreement with quasi-biennial oscillation (QBO) index at 30 mb calculated by NOAA/ESRL. Thus GWs with westward horizontal propagation are filtered by the westward QBO wind in the LS whereas GWs with eastward horizontal propagation can propagate upward and contribute to the eastward QBO wind in the LS above 22 km altitude. In addition, absorbed eastward waves contribute to the enhancement of the eastward wind in the middle troposphere when they propagate downward. Using radiosonde observations, Vincent and Alexander (2000) previously observed energy density maxima during QBO westward phase for convective GWs with intrinsic periods of 20–25 h, horizontal wavelengths of 200–2000 km (mean value of 100 km) and horizontal phase speed of about $10\,m\,s^{-1}$ in the

ACPD
13, 10757–10807, 2013

LS above Coco Island (12° S, 97° E). Recently, the analysis of SABER/TIMED data supports that QBO winds act as a significant filter in GW propagation depending on the QBO phases (Zhang et al., 2012). Kawatani et al. (2010) also demonstrated that small-scale GWs play an important role during the QBO westward phase in the LS.

Figure 10 shows the vertical cross section of the vertical velocity at 16° S of TC Ivan on 16 February at 12:00 UTC. The eyewall is characterized by strong updrafts with vertical velocity equal to 5–10 $m\,s^{-1}$ from 1 km altitude up to 15 km altitude. Perturbations with short horizontal wavelengths < 50 km are embedded on the iso-theta contours close to the area of strong updrafts on the east side of the TC in the UT. Downdrafts are well-observed in the TC eye, along the inner eyewall and on the east side of TC Ivan at altitudes of 8–12 km. The shape of the boundary of cloud reveals strong convection on the east side of the TC.

FFT is applied to time series of simulated vertical wind perturbations above the three meteorological stations (Gillot, Ivato, Tromelin) to analyze GW characteristics in the UT (12–16 km) and the LS (18–25 km) during the three stages of the TC:

- from 14 February to 15 February during the development stage of the system (hereafter called P1);
- from 15 February to 17 February during intensification (hereafter called P2);
- from 17 February to 18 February at 12:00 UTC during the landfall (hereafter called P3).

During P1, periods vary between 20 min to 3.5 h in the UT/LS above the three sites with a dominant period of about 20–30 min. During P2, similar periods are observed above Tromelin and Gillot. Secondary periods of 4–12 h are also present in the UT/LS above Ivato. In contrast, FFT spectra reveal dominant periods between 1 h and 12 h during P3. Observations above Tromelin and Gillot are consistent during P1 and P2 because of their location at the same latitude.

ACPD
13, 10757–10807, 2013

During the intense stage of TC Ivan on 16 February 2008, vertical flux of horizontal GW momentum increases in the UT above Tromelin (0.06 Nm^{-2}) and Reunion Island (0.08 Nm^{-2}). Sato (1993) estimated a maximum momentum flux of 0.04 Nm^{-2} at 20 km during TC Kelly (1987). Longitudinal series of horizontal pressure perturbations are filtered by a numeric monodimensional Butterworth filter to extract dominant GW modes with short (< 200 km) and medium (200–800 km) horizontal wavelengths on 16 February at 12:00 UTC at 20 km altitude (Fig. 11a and b). Figure 11a suggests an eastward phase propagation of the mode with 400–600 km horizontal wavelengths from the area of intense convection located north of the TC eye. Two-dimensional FFT is applied on binary image of pressure perturbations at the TC area. The bi-dimensional wavenumber space enables a multiscale analysis of the binary image and improves filtering from low to high frequencies. The FFT inverse provides reconstructed binary images for dominant modes. Constrast of filtered binary image is enhanced using contrast-limited adaptive histogram equalization (Zuiderveld, 1994). Figure 11c shows evidence of semi-circular patterns for medium modes. Black pixels in the upper left corner are attributed to processing side effects. Dominant modes of horizontal wavelengths of about 100–200 km are present in the south-east and north-east areas respectively (Fig. 11d). They are produced by strong convection in eastward propagating convective bands resulting from wavenumber-2 vortex Rossby waves located at northeast and southwest of the TC eye. FFT spectrum of vertical velocity provides dominant horizontal wavelengths of 20–80 km (peak at 60 km), 150 km, 180–250 km (peak at 200 km), 420–600 km (peak at 500 km) and 1000–2000 km (peak at 1250 km) at the latitude of TC eye in the LS. Most energy of observed modes is located at the latitude of TC eye (Fig. 12a). Large FFT amplitudes are displayed for short-scale waves (20–80 km) at the latitude of TC eye and longer scale waves (> 150 km) above TC area (9–21° S). This suggests that short-scale waves are high frequency modes with a dominant vertical propagation. Waves with 400–500 km horizontal wavelength are dominant above the TC basin. Figure 12b supports findings that observed modes are mainly located near the latitudes of TC eye. Long-scale modes have large latitudinal extension. Figure 12c

ACPD
13, 10757–10807, 2013

provides longitude-horizontal wavelength distribution derived from CWT of vertical velocity at the latitude of TC eye. It also supports the results about presence of modes with horizontal wavelengths < 2000 km associated with TC Ivan. Energy of high frequency modes (20–80 km) is dominant and confined at longitudes of 50–55° E near the TC eye. It peaks at 64 km horizontal wavelength at the location of the TC eye. Energy of medium-scale modes (100–800 km) with peaks at 150 km and 500 km horizontal wavelengths are secondary dominant. It is mainly observed east of the TC while energy of longer modes (1250 km) has a dominant horizontal extension west of the TC. Globally a longitudinal extension behind the TC is displayed for observed modes. This last figure complements that of ECMWF outputs especially for modes with horizontal wavelengths < 350 km. In addition, amplitudes of GWs are larger than those of ECMWF analyses. It suggests that GWs are better represented in Meso-NH simulation.

Similar modes are also observed in the horizontal wind, potential temperature and pressure. On 16 February at 12:00 UTC, horizontal wavelengths of GWs range between 40 and 60 km and between 300 km and 500 km with dominant periods of 1.2 h and 12–48 h (frequencies of $1.4 \times 10^{-3}\,s^{-1}$ and $1.39 \times 10^{-4}\,s^{-1}$–$0.3 \times 10^{-4}\,s^{-1}$). The linear GW dispersion relationship provides vertical wavelengths of about 1.5 km and 3.3 km respectively. Figure 13 displays a Hovmöller diagram of longitudinal pressure perturbations for modes with horizontal wavelengths between 200 and 800 km from 16 February at 12:00 UTC to 17 February at 18:00 UTC at latitude of 16° S. It reveals an eastward propagation of about 8–11 $m\,s^{-1}$ for medium modes in the LS.

6 Characteristics of TC rainbands

Spiral rainbands may produce severe rainfall outside the eyewall and play an important role in changing dynamic structure of TC structure, especially in the formation of concentric eyewalls (Wang and Wu, 2004; Hence and Houze, 2012). They can be triggered both by inertia–GWs (Willoughby, 1978) and vortex Rossby waves (Montgomery and Kallenbach, 1997). Mechanisms of spontaneous emission of spiral IG waves and

ACPD
13, 10757–10807, 2013

impacts on the angular momentum of TCs through outward spiral rainbands are discussed in Chow et al. (2002), Chow and Chan (2003) and Schecter (2008). Thus, recent studies demonstrate that wave-induced spiral rainbands affect TC intensity.

Characteristics of simulated TC rainbands are here analyzed from 15 February at 21:00 UTC to 17 February at 21:00 UTC. On 15 February at 21:00 UTC, a symmetry in TC rainbands is observed between east and west sides of the TC. The east–west (E–W) intensity ratio of maximum precipitation (IRMP) and the eye size are about 0.7 and 132 km respectively (Fig. 14a). On 16 February at 03:00 UTC, intensification of the eyewall of TC Ivan is accompanied with an intensification of precipitation at east side of the system. E–W IRMP and eye size are estimated about 2.8 and 100 km respectively (Fig. 14b). On 16 February at 06:00 UTC an asymmetry in TC rainbands is observed (Fig. 14c). The E–W IRMP decreases to about 1.4. Short rainbands of about 16 km wavelength appear at the eastern side of the TC.

Figure 13d shows a symmetry again on 16 February at 12:00 UTC with an IRMP of 1.1. A strong symmetry in TC rainbands is visualized on 16 February at 18:00 UTC with a TC eye size of 88 km (Fig. 14e). In addition many oscillations are visualized in precipitation. After the landfall of TC Ivan, a clear eye contraction is observed (eye size of 80 km) on 17 February at 12:00 UTC (Fig. 14f). When the west side of Ivan is above land, TC rainbands on west side are spread and less intense than those on east side above ocean. This is consistent with surface friction and latent heat release during landfall. Thus TC intensification is characterized by intense precipitation on the eastside. In addition E–W IRMP balance supports that TC rainbands play a role in TC energy dissipation. Tropical Rainfall Measuring Mission Precipitation near surface rate estimates at altitudes < 3 km visualized an asymmetry of TC eyewall in the eastern quadrant with the heaviest precipitation ($> 10\,\mathrm{mm\,h^{-1}}$) located north-east of the TC during intensification on 16 February at 0600 UT (Fig. 15). Large values are observed where wavenumber-1 vortex Rossby wave is located at north of TC eye. Figure 16 also shows evidence of a natural continuous and symmetrical eye contraction cycle during intensification and landfall stages. Mean size of TC eye is around 96 km. Globally, the

ACPD
13, 10757–10807, 2013

mean size of TC rainbands during the period of observation are 16 km, 24 km, 48 km and 60 km. Distance between TC rainbands are 24 km, 32 km, 56 km and 76 km. TC rainbands propagate outward at speed between 0.5 $m s^{-1}$ and 3 $m s^{-1}$. Thus the order of magnitude of the spacing and size of the rain bands are close to horizontal wavelengths of observed high-frequency GWs. Nevertheless, we should be cautious on the connection between GW horizontal wavelengths and radial spacing of rainbands. Figure 10 shows the presence of wavelike structures on clouds at altitudes of 4–8 km with horizontal wavelengths of about 30–40 km at longitudes of 54–55° E. Wind perturbations verify GW polarization relation. Modes with similar spectral characteristics are also observed in the LS (Fig. 12c).

7 Summary and conclusions

Characteristics of GWs were examined in the UT and the LS during the evolution of TC Ivan (2008) in the SWIO. Radiosonde and GPS RO data capture dominant low-frequency and quasi-inertia GWs with horizontal and vertical wavelengths of 80–400 km and 0.7–3 km respectively. Quasi-inertia GW modes with horizontal and vertical wavelengths of 350–1000 km and 1–2 km respectively were derived from ECMWF analyses behind TC Ivan in the LS. ECMWF analyses also showed presence of GWs with long horizontal and vertical wavelengths of 1400–1700 km and 5–10 km respectively and periods of 1–2 days. A large continuous spectrum of GWs with horizontal wavelengths between 350 km and 1000 km is observed east of TC eye.

Meso-NH simulations provided more detailed information about the activity of TC-related GWs during the development stage, intensification and landfall. Model outputs revealed presence of high and low frequency GWs (periods of 20 min–2 days) with short and medium horizontal wavelengths of 40–800 km and short vertical wavelengths of 1.5–3.3 km. Observations and model outputs showed evidence of a dominant quasi-inertia GW mode closely linked to TC Ivan with horizontal and vertical wavelengths of

ACPD
13, 10757–10807, 2013

400–800 km and 1.5–3.5 km with eastward horizontal propagation of about 10 m s^{-1} during intensification.

A strong localized convective source resulting from wavenumber-1 vortex Rossby wave located in the upper part of the TC was suggested as a source of observed semi-circular wave structures in model outputs during intensification stage of TC Ivan. In addition eastward propagating convective bands resulting from wavenumber-2 vortex Rossby waves could be responsible of short scale GWs. FFT and CWT also revealed high-frequency modes with a dominant horizontal wavelength of 64 km.

Results also support that some GWs-related to TC could be filtered out by the background wind and contribute locally to the QBO forcing in the LS. A strong activity of GWs was also observed during landfall accompanied with the enhancement of eastward wind in the middle troposphere probably because of absorbed eastward propagating GWs as they propagate downward. In addition characteristics of TC rainbands revealed intensification of TC eyewall with strong precipitation at east side of TC Ivan during intensification. Distance between TC rainbands were similar to short wavelengths of observed GWs. Meso-NH simulation also revealed high-frequency GWs-related TC-clouds in the troposphere on 16 February and a natural continuous and symmetrical eye contraction cycle during intensification and landfall stages of TC Ivan.

Results are consistent with previous observational studies on characteristics of TC-related GWs (Chane Ming et al., 2002, 2010) and link between GW energy density and TC activity in the UT/LS (Ibrahim et al., 2010). Chane Ming et al. (2010) also detected dominant eastward propagating modes with a horizontal wavelength of about 500 km in the UT/LS during intense TC Dina (2002) in the SWIO and TC Faxai (2001) in north-west Pacific Ocean with prevailing westward wind between altitudes of 10–22 km and eastward QBO above. An increase in total energy density of about 30 % of the climatological energy density in austral summer was estimated in the LS above Tromelin during TC Dina.

From numerical simulations, Kim et al. (2005, 2009) analyzed low frequency GWs with medium horizontal wavelengths of 300–600 km, a vertical wavelength of 3–11 km,

ACPD
13, 10757–10807, 2013

and a period of 6–11 h during a category 4 TCs Rusa (2002) and Ewiniar (2006) in the LS. Convection in the TC-generated cloud bands was suggested to be a major source of GWs during TC Rusa. Dominant eastward propagating stratospheric waves were observed during the mature stage of TC Ewiniar. In contrast, Kuester et al. (2008) simulated high frequency GWs with horizontal wavelengths of 15–300 km, vertical wavelengths of 4–8 km, and intrinsic periods of 20–100 min above a category 2 TC Humberto (2001). Kim and Chun (2010) examined eastward propagating GWs with horizontal wavelengths of 10–100 km and periods less than 2 h produced by a category 5 TC Saomai (2006). Waves with horizontal wavelengths > 80 km and periods > 1 h are found to be the dominant contribution to the momentum flux. More recently, Chen et al. (2012) numerically investigated eastward propagating GWs with long horizontal scales of about 1000 km generated by TC Matsa (2005) in the LS. Three major mechanisms, i.e. mechanical oscillator effect (Fovell et al., 1992), obstacle effect (Clark et al., 1986), and thermal heating effect (Salby and Garcia, 1987) were suggested not be sufficient to explain generation of such GWs (Chen et al., 2012). Recent numerical studies suggest that weakening of simulated TCs is closely associated with these environmentally induced asymmetries that develop in the vicinity of the TC eyewall (Wu and Braun, 2004). Movement of storm through the surrounding atmosphere and the wind shear are major causes of an asymmetric distribution of rainband structures (Reasor et al., 2000; Houze, 2010). In a low shear environment, rainfall is mainly ahead of a storm, especially in the outer rainband regions otherwise it is located downshear left (right) in the northern (southern) hemisphere (Wu and Braun, 2004). When TC intensity increases, the asymmetry maximum shifts upwind to the left in the Northern Hemisphere.

Previously, asymmetries in surface friction caused by vortex translation were suggested to produce a wavenumber-1 asymmetry in convergence (Shapiro, 1983). Asymmetric forcing has also been studied as a possibly important intensification mechanism. Eyewall convection can be enhanced and shifted inward on one side by inflow associated with the vortex Rossby waves in the lower troposphere, while it is suppressed and shifted outward on the other side by outflow (Wang, 2002a). Asymmetries can trans-

ACPD
13, 10757–10807, 2013

port energy to the outside of the eyewall due to their nature of the vortex Rossby waves (Montgomery and Kalenbach, 1997). Eyewall asymmetries interact with the mean vortex through eddy momentum fluxes and partially extract their kinetic energy form the mean vortex, leading to weakening of the mean tangential and radial winds (Houze et al., 2006). If TC asymmetries become sufficiently strong, then air with high values of potential vorticity and equivalent potential temperature are mixed outward and cause the weakening of the warm core aloft and the increase of central pressure (Frank and Ritchie, 2001). Radial maximum wind can also be accelerated during intensification stage and produce an eyewall contraction (Houze et al., 2006) which was observed in the present study. The environmental shear induced by land-sea contrast was also revealed to produce highly structures in landfalling TC, responsible of the distribution of the strongest wind and the heaviest rainfall (Chen and Yau, 2003). An asymmetry first occurs at the top of the vortex and propagates to the surface. Rainfall is generally observed to have a maximum ahead of the TC centre which indicates importance of surface friction induced by low level convergence. Thus observations and numerical simulations have suggested vortex Rossby waves to be related to changes in the structure and intensity of TCs (Wang, 2002b). In addition, outward propagation of wavenumber-1 Rossby waves is believed to initiate inner spiral rainbands. During storm intensity change, shearing deformation can stretch vorticity into filaments that spiral toward the centre of the TC (Houze et al., 2006). In addition, Chow et al. (2002) show that fluctuation of the PV distribution in the TC core region can act as a source, generating gravity waves that produce banded structures and the moving spiral rainbands. Chen et al. (2006) showed that during austral summer when TC s are active in the Southern Hemisphere, vertical wind shear is mostly weak and moderate ($< 15\,m\,s^{-1}$) and that TCs display the largest asymmetries. In our study the contrast wind shear enhanced by land-sea contrast is suggested to be responsible of the observed wavenumber-1 asymmetry during intensification stage just before landfall of TC Ivan. In conclusion, Meso-NH model proved to be a useful numerical tool to explore a wide ranged spectrum of TC-related GWs in the UT/LS in relation with a realistic TC dynamics. Further

ACPD
13, 10757–10807, 2013

studies should include detailed descriptions of TC-related GW sources, GW anisotropic propagation and GW effects on the rainband characteristics and the background wind.

Acknowledgements. This work was financially supported by La Région Réunion and the European Union, and by the Fondation MAIF through the PRECYP project. The authors also thank Meso-NH team at Météo-France and Laboratoire d'Aérologie for source code and assistance. Meso-NH model was run on supercomputers of University of La Réunion and Météo-France.

The publication of this article is financed by CNRS-INSU.

References

Alexander, M. J.: Parameterization of physical processes: gravity wave momentum fluxes, Encyclopedia of the Atmospheric Sciences, Academic/Elsevier, London, 1699–1705, 2003.

Alexander, M. J., Geller, M., McLandress, C., Polavarapu, S., Preusse, P., Sassi, F., Sato, K., Eckermann, S., Ern, M., Hertzog, A., Kawatani, Y., Pulido, M., Shaw, T., Sigmond, M., Vincent, R., and Watanabe, S.: Recent developments in gravity wave effects in climate models, and the global distribution of gravity wave momentum flux from observations and models, Q. J. Roy. Meteor. Soc., 136, 1103–1124, 2010.

Alexander, S. P., Tsuda, T., Kawatani, Y., and Takahashi, M.: Global distribution of atmospheric waves in the equatorial upper troposphere and lower stratosphere: COSMIC observations of wave mean flow interactions, J. Geophys. Res., 113, D24115, doi:10.1029/2008JD010039, 2008.

Anthes, R. A.: Exploring Earth's atmosphere with radio occultation: contributions to weather, climate and space weather, Atmos. Meas. Tech., 4, 1077–1103, doi:10.5194/amt-4-1077-2011, 2011.

ACPD
13, 10757–10807, 2013

Baldwin, M. P., Gray, L. J., Dunkerton, T. J., Hamilton, K., Haynes, P. H., Randel, W. J., Holton, J. R., Alexander, M. J., Hirota, I., Horinouchi, T., Jones, D. B. A., Kinnersley, J. S., Marquardt, C., Sato, K., and Takahashi, M.: The Quasi-Biennial oscillation, Rev. Geophys., 39, 179–229, doi:10.1029/1999RG000073, 2001.

Bechtold, P., Bazile, E., Guichard, F., Mascart, P., and Richard, E.: A mass flux convection scheme for regional and global models, Q. J. Roy. Meteorol. Soc., 127, 869–886, 2001.

Chaboureau, J.-P., Cammas, J.-P., Mascart, P., Pinty, J.-P., Claud, C., Roca, R., and Morcrette, J.-J.: Evaluation of a cloud system life-cycle simulated by Meso-NH during FASTEX using METEOSAT radiances and TOVS-3I cloud retrievals, Q. J. Roy. Meteorol. Soc., 126, 1735–1750, 2000.

Chane Ming, F., Molinaro, F., and Leveau, J.: Wavelet techniques applied to lidar signal in the analysis of the middle atmosphere dynamics, Appl. Sig. Process., 6, 95–106, 1999.

Chane-Ming, F., Roff, G., Robert, L., and Leveau, J.: Gravity wave characteristics over Tromelin Island during the passage of cyclone Hudah, Geophys. Res. Lett., 29,18-1–18-4, doi:10.1029/2001GL013286, 2002.

Chane-Ming, F., Faduilhe, D., and Leveau, J.: Latitudinal and seasonal variability of gravity-wave energy in the South–West Indian Ocean, Ann. Geophys., 25, 2479–2485, doi:10.5194/angeo-25-2479-2007, 2007.

Chane Ming, F., Chen, Z., and Roux, F.: Analysis of gravity-waves produced by intense tropical cyclones, Ann. Geophys., 28, 531–547, doi:10.5194/angeo-28-531-2010, 2010.

Chen, D., Chen, Z. Y., and Lü, D. R.: Simulation of the stratospheric gravity waves generated by the Typhoon Matsa in 2005, Sci. China Earth Sci., 55, 602–610, doi:10.1007/s11430-011-4303-1, 2012.

Chen, S. S., Knaff, J. A., and Marks, F. D.: Effects of vertical wind shear and storm motion on tropical cyclone rainfall asymmetries deduced from TRMM, Mon. Weather Rev., 134, 3190–3208, 2006.

Chen, Y. and Yau, M. K.: Asymmetric structures in a simulated landfall hurricane, J. Atmos. Phys., 60, 2294–2312, 2003.

Chow, K. C. and Chan, K. L.: Angular momentum transports by moving spiral waves, J. Atmos. Sci., 60, 2004–2009, 2003.

Chow, K. C., Chan, K. L., and Lau, A. K. H.: Generation of moving spiral bands in tropical cyclones, J. Atmos. Sci., 59, 2930–2950, 2002.

ACPD
13, 10757–10807, 2013

Clark, T. L., Hauf, T., and Kuettner, J. P.: Convectively forced internal gravity waves: Results from two-dimensional numerical experiments, Q. J. Roy. Meteor. Soc., 112, 899–925, 1986.
Cuxart, J., Bougeault, P., and Redelsperger, J.-L.: A turbulence scheme for mesoscale and large-eddy simulations, Q. J. Roy. Meteor. Soc., 126, 1–30, 2000.
Das, S. S., Uma, K. N., and Das, S. K.: MST radar observations of short-period gravity wave during overhead tropical cyclone, Radio Sci., 47, RS2019, doi:10.1029/2011RS004840, 2012.
Dhaka, S. K., Takahashi, M., Shibagaki, Y., Yamanaka, M. D., and Fukao, S.: Gravity wave generation in the lower stratosphere due to passage of the Typhoon 9426 (Orchid) observed by the MU radar at Shigaraki (34.85° N, 136.10° E), J. Geophys. Res., 108, 4595, doi:10.1029/2003JD003489, 2003.
Dewan, E. M., Picard, R. H., O'Neil, R. R., Gardiner, H. A., Gibson, J., Mill, J. D., Richards, E., Kendra, M., and Gallery, W. O.: MSX satellite observations of thunderstorm-generated gravity waves in mid-wave infrared images of the upper stratosphere, Geophys. Res. Lett., 25, 939–942, 1998.
Dunkerton, T. J.: Theory of the mesopause semiannual oscillation, J. Atmos. Sci., 39, 2681–2690, 1982.
Ern, M. and Preusse, P.: Gravity wave momentum flux spectra observed from satellite in the summertime subtropics: Implications for global modeling, Geophys. Res. Lett., 39, L15810, doi:10.1029/2012GL052659, 2012.
Fovell, R., Durran, D., and Holton, J. R.: Numerical simulations of convectively generated stratospheric gravity waves, J. Atmos. Sci., 49, 1427–1442, 1992.
Frank, W. M. and Ritchie, E. A.: Effects of vertical wind shear on the intensity and structure of numerically simulated hurricanes, Mon. Weather Rev., 129, 2249–2269, 2001.
Fritts, D. C. and Alexander, M. J.: Gravity wave dynamics and effects in the middle atmosphere, Rev. Geophys., 41, 1003, doi:10.1029/2001RG000106, 2003.
Gill, A. E.: Atmosphere-Ocean Dynamics, Academic Press, Inc., New York, USA, 662 pp., 1982.
Gregory, D., Morcrette, J.-J., Jakob, C., Beljaars, A. C. M., and Stockdale, T.: Revision of convection, radiation and cloud schemes in the ECMWF integrated forecasting system, Q. J. Roy. Meteor. Soc., 126, 1685–1710, 2000.
Healy, S. B.: Operational assimilation of GPS radio occultation measurements at ECMWF, available online at: http://www.ecmwf.int/publications/newsletters/pdf/111.pdf, ECMWF Newsletter, 111, 6–11, 2007.

ACPD
13, 10757–10807, 2013

Healy, S. B. and Thepaut, J. N.: Assimilation experiments with CHAMP GPS radio occultation measurements, Q. J. Roy. Meteor. Soc., 132, 605–623, doi:10.1256/qj.04.182, 2006.
Hence, D. A. and Houze, R. A.: Vertical structure of tropical cyclone rainbands as seen by the TRMM precipitation radar, J. Atmos. Sci., 69, 2644–2661, 2012.
Hendricks, E. A., Schubert, W. H., Fulton, S. R., and McNoldy, B. D.: Spontaneous-adjustment emission of inertia-gravity waves by unsteady vortical motion in the hurricane core, Q. J. Roy. Meteor. Soc., 136, 537–548, 2008.
Hendricks, E. A., McNoldy, B. D., and Schubert, W. H.: Observed inner core structural variability in hurricane Dolly (2008), Mon. Weather Rev., 140, 4066–4077, 2012.
Horinouchi, T., Nakamura, T., and Kosaka, J.: Convectively generated mesoscale gravity waves simulated throughout the middle atmosphere, Geophys. Res. Lett., 29, 2007, , doi:10.1029/2002GL016069, 2002.
Houze, R. A.: Clouds in tropical cyclones, Mon. Weather Rev., 138, 293–344, 2010.
Houze, R. A., Cetrone, J., Brodzik, S. R., Chen, S. S., Zhao, W., Lee, W.-C., Moore, J. A., Stossmeister, G. J., Bell, M. M., and Rogers, F. F.: The hurricane rainband and intensity change experiment: observations and modeling of hurricanes Katrina, Ophelia, and Rita, B. Am. Meteorol. Soc., 87, 1503–1521, 2006.
Huang, C.-Y., Kuo, Y.-H., Chen, S.-Y., Terng, C.-T., Chien, F.-C., Lin, P.-L., Kueh, M.-T., Chen, S.-H., Yang, M.-J., Wang, C.-J., and Rao, A. S. K. A. P.: Impact of GPS radio occultation data assimilation on regional weather predictions, GPS Solut., 14, 35–49, doi:10.1007/s10291-009-0144-1, 2010.
Ibrahim, C., Chane Ming, F., Barthe, C., and Kuleshov, Y: Diagnosis of tropical cyclone activity through gravity wave energy density in the South West Indian Ocean, Geophys. Res. Lett., 37, L09807, doi:10.1029/2010GL042938, 2010.
Jolivet, S., Chane Ming, F., Barbary, D., and Roux, F.: A numerical study of orographic forcing on TC Dina (2002) in South West Indian Ocean, Ann. Geophys., 31, 107–125, doi:10.5194/angeo-31-107-2013, 2013.
Kain, J. S. and Fritsch, J. M.: A One-dimensional entraining/detraining plume model and its application in convective parameterization, J. Atmos. Sci., 47, 2784–2802, 1990.
Kawatani, Y., Watanabe, S., Sato, K., Dunkerton, T. J., Miyahara, S., and Takahashi, M.: The roles of equatorial trapped waves and internal inertia-gravity waves in driving the Quasi-Biennial oscillation, Part I: Zonal mean wave forcing, J. Atmos. Sci., 67, 963–980, doi:10.1175/2009JAS3222.1, 2010.

ACPD
13, 10757–10807, 2013

Kim, S.-Y. and Chun, H.-Y.: Stratospheric gravity waves generated by Typhoon Saomai (2006): numerical modeling in a moving frame following the typhoon, J. Atmos. Sci., 67, 3617–3636, doi:10.1175/2010JAS3374.1, 2010.
Kim, S.-Y. and Chun, H.-Y.: Impact of typhoon-generated gravity waves in the typhoon development, Geophys. Res. Lett., 38, L01806, doi:10.1029/2010GL045719, 719, 2011.
Kim, S.-Y., Chun, H.-Y., and Baik, J.-J.: A numerical study of gravity waves induced by convection associated with Typhoon Rusa, Geophys. Res. Lett., 32, L24816, doi:10.1029/2005GL024662, 2005.
Kim, S.-Y., Chun, H.-Y., and Wu, D. L.: A study on stratospheric gravity waves generated by Typhoon Ewiniar: numerical simulations and satellite observations, J. Geophys. Res., 114, D22104, doi:10.1029/2009JD011971, 2009.
Kim, Y.-J. and Chun, H.-Y.: A computationally efficient non stationary convective gravity-wave drag parameterization for global atmospheric prediction systems, Geophys. Res. Lett., 32, L22805, doi:10.1029/2005GL024572, 2005.
Kim, Y.-J., Eckermann, S. E., and Chun, H.-Y.: An overview of the past, present and future of gravity-wave drag parameterization for numerical climate and weather prediction models, Atmos. Ocean, 41, 65–98, 2003.
Kuester, M. A., Alexander, M. J., and Ray, E. A.: A model study of gravity waves over Hurricane Humberto (2001), J. Atmos. Sci., 65, 3231–3246, 2008.
Kunii, M., Seko, H., Ueno, M., Shoji, Y., and Tsuda, T.: Impact of Assimilation of GPS radio occultation refractivity on the forecast of Typhoon Usagi in 2007, J. Meteorol. Soc. Jap., 90, 255–273, doi:10.2151/jmsj.2012-207, 2012.
Lafore, J. P., Stein, J., Asencio, N., Bougeault, P., Ducrocq, V., Duron, J., Fischer, C., Héreil, P., Mascart, P., Masson, V., Pinty, J. P., Redelsperger, J. L., Richard, E., and Vilà-Guerau de Arellano, J.: The Meso-NH Atmospheric Simulation System. Part I: adiabatic formulation and control simulations, Ann. Geophys., 16, 90–109, doi:10.1007/s00585-997-0090-6, 1998.
Lane, T. P. and Knievel, J. C.: Some effects of model resolution on simulated gravity waves generated by deep, mesoscale convection, J. Atmos. Sci., 62, 3408–3419, doi:10.1175/JAS, 2005.
Lane, T. P. and Reeder, M. J.: Modelling the generation of gravity waves by a maritime continent thunderstorm, Q. J. Roy. Meteor. Soc., 127, 2705–2724, 2001.

ACPD
13, 10757–10807, 2013

Leclaire De Bellevue, J., Baray, J. L., Baldy, S., Ancellet, G., Diab, R., and Ravetta, F.: Simulations of stratospheric to tropospheric transport during the tropical cyclone Marlene event, Atmos. Env., 41, 6510, doi:10.1016/j.atmosenv.2007.04.040, 2007.

Lin, C.-Y., Hsu, H.-M., Sheng, Y.-F., Kuo, C.-H., and Liou, Y.-A.: Mesoscale processes for super heavy rainfall of Typhoon Morakot (2009) over Southern Taiwan, Atmos. Chem. Phys., 11, 345–361, doi:10.5194/acp-11-345-2011, 2011.

Liou, Y.-A., Pavelyev, A. G., Huang, C.-Y., Igarashi, K., Hocke, K., and Yan, S.-K.: Analytic method for observation of the gravity waves using radio occultation data, Geophys. Res. Lett., 30, 2021, doi:10.1029/2003GL017818, 2003.

Liou, Y.-A., Pavelyev, A. G., Wicker, J., Liu, S. F., Pavelyev, A. A., Schmidt, T., and Igarashi, K.: Application of GPS radio occultation method for observation of the internal waves in the atmosphere, J. Geophys. Res., 111, D06104, doi:10.1029/2005JD005823, 2006.

Liou, Y.-A., Pavelyev, A. G., Matyugov, S. S., Yakovlev, O. I., and Wickert, J.: Radio Occultation Method for Remote Sensing of the Atmosphere and Ionosphere, INTECH, Vukovar, Croatia, 170 pp., 2010.

Liu, H., Anderson, J, and Kuo, Y.-H.: Improved analyses and forecasts of Hurricane Ernesto's genesis using radio occultation data in an ensemble filter assimilation system, Mon. Weather Rev., 140, 151–166, doi:10.1175/MWR-D-11-00024.1, 2012.

Liu, Y., Zhang, D.-L., and Yau, M. K.: A multiscale numerical study of hurricane Andrew (1992), Part II: Kinematics and inner-core structures, Mon. Weather Rev., 127, 2597–2616, 1999.

Marks, F. D., Houze, R. A., and Gamache, J. F.: Dual-aircraft investigation of the inner core of hurricane Norbert, Part I: Kinematic structure, J. Atmos. Sci., 49, 919–942, 1992.

Montgomery, M. T. and Kallenbach, R. J.: A theory for vortex Rossby-waves and its application to spiral bands and intensity changes in hurricanes, Q. J. Roy. Meteor. Soc., 123, 435–465, 1997.

Montroty, R., Rabier, F., Westrelin, S., Faure, G., and Viltard, N.: Impact of wind bogus and cloud and rain affected SSM/I data on tropical cyclones analyses and forecasts, Q. J. Roy. Meteor. Soc., 134, 1673–1699, 2008.

Niranjan Kumar, K., Ramkumar, T. K., and Krishnaiah, M.: MST radar observation of inertia-gravity waves generated from tropical cyclones, J. Atmos. Sol. Terr. Phys., 73, 1890–1906, 2011.

ACPD
13, 10757–10807, 2013

Nuissier, O., Rogers, R. F., and Roux, F.: A numerical simulation of hurricane Bret on 22–23 August 1999 initialized with airborne Doppler radar and dropsonde data, Q. J. Roy. Meteor. Soc., 131, 155–194,doi:10.1256/qj.02.233, 2006.

Pfister, L., Chan, K. R., Bui, T. P., Bowen, S., Legg, M., Gary, B., Kelly, K., Proffitt, M., and Starr, W.: Gravity waves generated by a tropical cyclone during the step tropical field programm: a case study, J. Geophys. Res., 98, 8611–8638, 1993.

Piani, C., Durran, D., Alexander, M. J., and Holton, J. R.: A numerical study of three-dimensional gravity waves triggered by deep tropical convection and their role in the dynamics of the QBO, J. Atmos. Sci., 57, 3689–3702, 2000.

Pinty, J.-P., and Jabouille, P.: A mixed-phase cloud parameterization for use in mesoscale non-hydrostatic model: simulations of a squall line and of orographic precipitations, Proc. Conf. of Cloud Physics, Everett, WA, USA, Am. Meteorol. Soc., 217–220, 1999.

Pirscher, B., Foelsche, U., Borsche, M., Kirchengast, G., and Kuo, Y.-H.: Analysis of migrating diurnal tides detected in FORMOSAT-3/COSMIC temperature data, J. Geophys. Res., 115, D14108, doi:10.1029/2009JD013008, 2010.

Plougonven, R. and Teitelbaum, P. H.: Comparison of a large-scale inertia gravity wave as seen in the ECMWF analyses and from radio-sondes, Geophys. Res. Lett., 30, 1954, doi:10.1029/2003GL017716, 2003.

Preusse, P., Eckermann, S. D., and Ern, M.: Transparency of the atmosphere to short horizontal wavelength gravity waves, J. Geophys. Res., 113, D24104, doi:10.1029/2007JD009682, 2008.

Reasor, P. D., Montgomery, M. T., Marks, F. D., and Gamache, J. F.: Low-wavenumber structure and evolution of the hurricane inner core observed by airborne dual-Doppler radar, Mon. Weather Rev., 128, 1653–1680, 2000.

Richter, J. H., Sassi, F., and Garcia, R. R.: Toward a physically based gravity wave source parameterization in a general circulation model, J. Atmos. Sci., 67, 136–156, 2010.

Roux, F., Chane-Ming, F., Lasserre-Bigorry, A., and Nuissier, O.: Structure and evolution of intense tropical cyclone Dina near La Réunion on 22 January 2002: GB-EVTD analysis of single Doppler radar observations, J. Atmos. Oceanic. Technol., 21, 1501–1518, 2004.

Salby, M. L. and Garcia, R. R.: Transient response to localized episodic heating in the tropics, Part I: Excitation and short-time near-field behavior, J. Atmos. Sci., 44, 458–498, 1987.

Sato, K.: Small-scale wind disturbances observed by the MU radar during the passage of Typhoon Kelly, J. Atmos. Sci., 50, 518–537, 1993.

ACPD
13, 10757–10807, 2013

Saunders, R., Matricardi, M., Brunel, P., English, S., Bauer, P., O'Keeffe, U., Francis, P., and Rayer, P.: RTTOV-8 science and validation report, NWP SAF report, Met Office, Exeter, UK, 41 pp., 2005.
Schecter, D. A.: The spontaneous imbalance of an atmospheric vortex at high Rossby number, J. Atmos. Sci., 65, 2498–2521, 2008.
Schroeder, S., Preusse, P., Ern, M., and Riese, M.: Gravity waves resolved in ECMWF and measured by SABER, Geophys. Res. Lett., 36, L10805, doi:10.1029/2008GL037054, 2009.
Schubert, W. H., Rozoff, C. M., Vigh, J. L., McNoldy, B. D., and Kossin, J. P.: On the distribution of subsidence in the hurricane eye, Q. J. Roy. Meteor. Soc., 133, 595–605, 2007.
Shapiro, L. J.: The asymmetric boundary layer flow under a translating hurricane, J. Atmos. Sci., 40, 1984–1998, 1983.
Shutts, G. J. and Vosper, S. B.: Stratospheric gravity waves revealed in NWP model forecasts, Q. J. Roy. Meteor. Soc., 137, 303–317, doi:10.1002/qj.7, 2011.
Sun, B., Reale, A., Seidel, D. J., and Hunt, D. C.: Comparing radiosonde and COSMIC atmospheric profile data to quantify differences among radiosonde types and the effects of imperfect collocation on comparison statistics, J. Geophys. Res., 115, D23104, doi:10.1029/2010JD014457, 2010.
Vincent, R. A. and Alexander, M. J.: Gravity waves in the tropical lower stratosphere: an observational study of seasonal and interannual variability, J. Geophys. Res., 105, 17971–17982, doi:10.1029/2000JD900196, 2000.
Wang, Y.: Vortex Rossby waves in a numerically simulated tropical cyclone, Part I: Overall structure, potential vorticity and kinetic energy budgets, J. Atmos. Sci., 59, 1213–1238, 2002a.
Wang, Y.: Vortex Rossby waves in a numerically simulated tropical cyclone, Part II: The role in tropical cyclone structure and intensity changes, J. Atmos. Sci., 59, 1239–1262, 2002b.
Wang, Y. and Wu, C.-C.: Current understanding of tropical cyclone structure and intensity changes – a review, Meteor. Atmos. Phys., 87, 257–278, 2004.
Willoughby, H. E.: A possible mechanism for the formation of hurricane rainbands, J. Atmos. Sci., 35, 838–848, 1978.
Xiao, C. Y. and Hu, X.: Analysis on the global morphology of stratospheric gravity wave activity deduced from the COSMIC GPS occultation profiles, GPS solutions, 14, 65–74, doi:10.1007/s10291-009-0146-z, 2010.

ACPD
13, 10757–10807, 2013

Zhang, D.-L., Liu, Y. B., and Yau, M. K.: A multiscale numerical study of Hurricane Andrew (1992), Part III: Dynamically induced vertical motion, Mon. Weather Rev., 128, 3772–3788, 2000.

Zhang, D.-L., Liu, Y. B., and Yau, M. K.: A multiscale numerical study of hurricane Andrew (1992), Part IV: Inner-core thermodynamics, Mon. Weather Rev., 130, 2745–2763, 2002.

Zhang, K., Fu, E., Silcock, D., Wang, Y., and Kuleshov, Y.: An investigation of atmospheric temperature profiles in the Australian region using collocated GPS radio occultation and radiosonde data, Atmos. Meas. Tech., 4, 2087–2092, doi:10.5194/amt-4-2087-2011, 2011.

Zhang, Y., Xiong, J., Liu, L., and Wan, W.: A global morphology of gravity wave activity in the stratosphere revealed by the 8-yr SABER/TIMED data, J. Geophys. Res., 117, D21101, doi:10.1029/2012JD017676, 2012.

Zuiderveld, K.: Contrast limited adaptive histogram equalization, in: Graphics Gems IV, edited by: Heckbert, P., Academic Press, ISBN 0-12-336155-9, Academic Press Professional, San Diego, USA, 474–485, 1994.

ACPD

13, 10757–10807, 2013

Table 1. Spectral characteristics of GWs above radiosonde stations of Gillot and Ivato from 15 to 18 February 2008 (λ_h and λ_v: horizontal and vertical wavelengths).

Station (altitude)	Number of profiles	Intrinsic period (h)	λ_h (km)	λ_v(km)
Gillot (10–15 km)	4	7, 4	84, 210	1, 2.6
Gillot (18–22 km)	3	13	130, 390	0.68, 2.1
Ivato (10–15 km)	6	4, 6	66, 130	1.7, 2.6

ACPD
13, 10757–10807, 2013

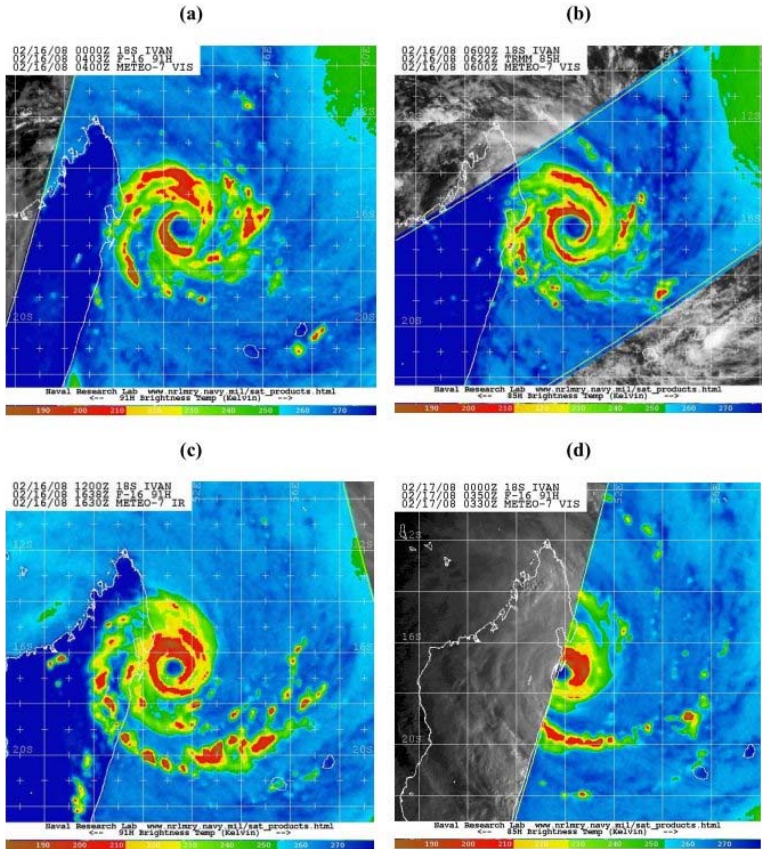

Fig. 1. METEOSAT7 visible images of TC Ivan with **(a)** F-16 SSMI/S brightness temperatures on 16 February 2008 at 00:00 UTC **(b)** TRMM TMI brightness temperatures at 85 H on 16 February 2008 at 06:00 UTC **(c)** F-16 SSMI/S brightness temperatures on 16 February 2008 at 16:30 UTC **(d)** F-16 SSMI/S brightness temperatures on 17 February 2008 at 00:00 UTC (from http://www.nrlmry.navy.mil/tc_pages).

ACPD
13, 10757–10807, 2013

Observation and a numerical study of gravity waves

F. Chane Ming et al.

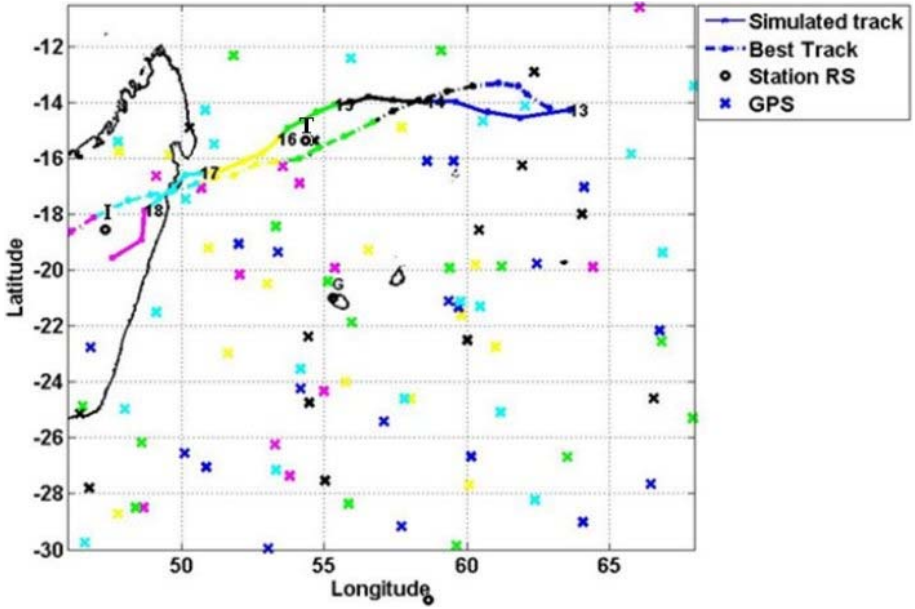

Fig. 2. TC Ivan best track data (RSMC La Reunion, solid line) and cyclone track data obtained by simulation (Meso-NH, dashed line). Crosses indicate locations of GPS RO soundings and black circles correspond to locations of meteorological stations (G: Gillot, I: Ivato, T: Tromelin). Colours of crosses and segments of tracks indicate the day (13 February – navy blue; 14 February – black; 15 February – green; 16 February – yellow; 17 February – light blue and 18 February – magenta).

ACPD
13, 10757–10807, 2013

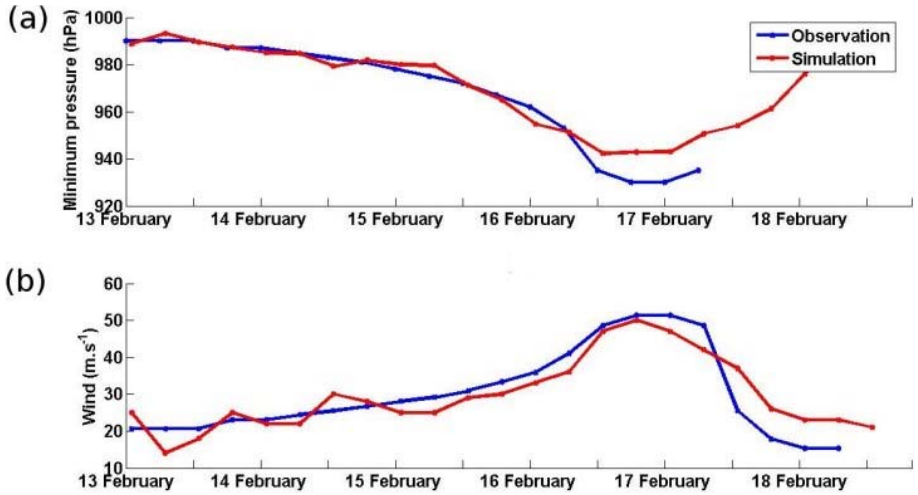

Fig. 3. Time series of **(a)** the minimum central pressure (hPa) and **(b)** the 10 min average maximum sustained winds speed ($m\,s^{-1}$) from best track data (blue line) and model simulation (red line).

ACPD
13, 10757–10807, 2013

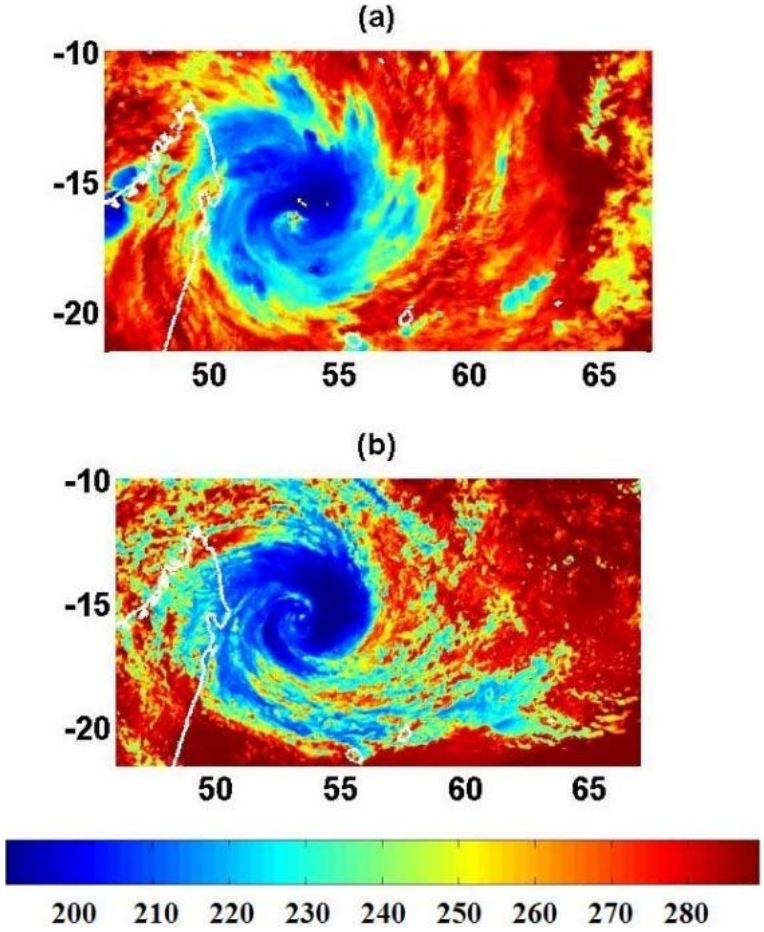

Fig. 4. Brightness temperature (K) from **(a)** IR channel of Meteosat-7 and **(b)** Meso-NH outputs on 16 February 2008 at 00:00 UTC.

ACPD
13, 10757–10807, 2013

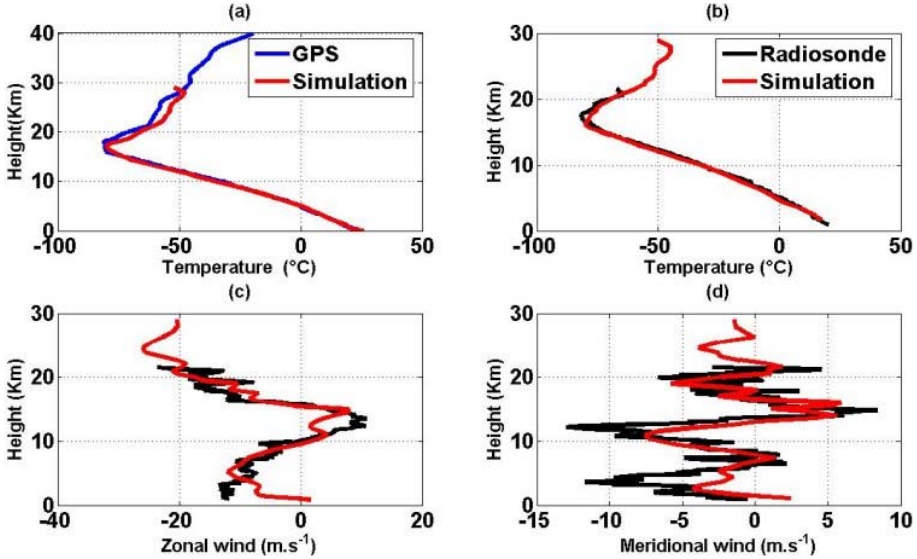

Fig. 5. Observed (black – radiosonde, blue – GPS) and simulated (red) vertical profiles of: **(a)** temperature from GPS RO at (19° S, 59° E) on 15 February at 00:26 UTC (00:00 UTC), **(b)** temperature of radiosonde at Gillot on 16 February at 11:12 UTC (12:00 UTC), and **(c)** and **(d)** radiosonde zonal wind and meridional wind at Gillot on 16 February 2008 at 11:12 UTC.

ACPD
13, 10757–10807, 2013

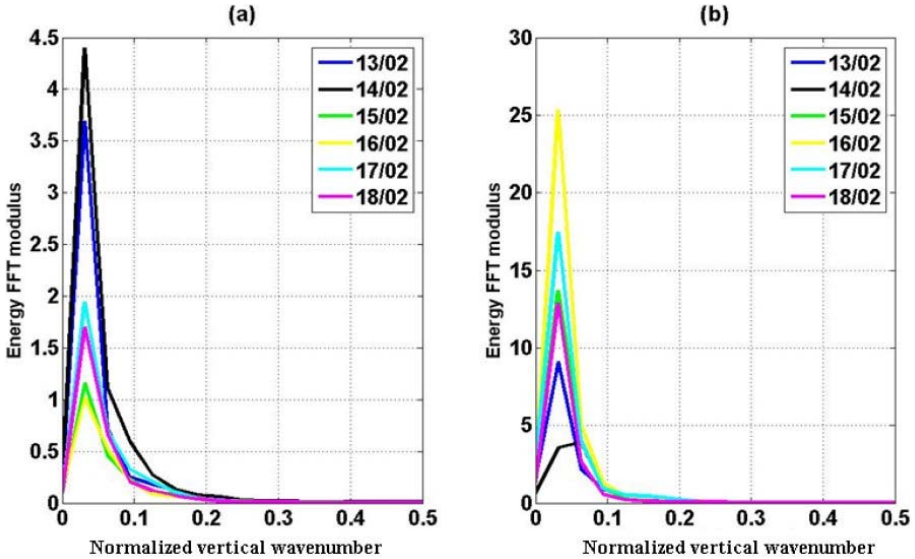

Fig. 6. Fast Fourier transform spectra of 70 GPS RO temperature perturbations from 13 February to 18 February 2008 in **(a)** the UT and **(b)** the LS (λ_v = 100 m/normalized frequency).

ACPD
13, 10757–10807, 2013

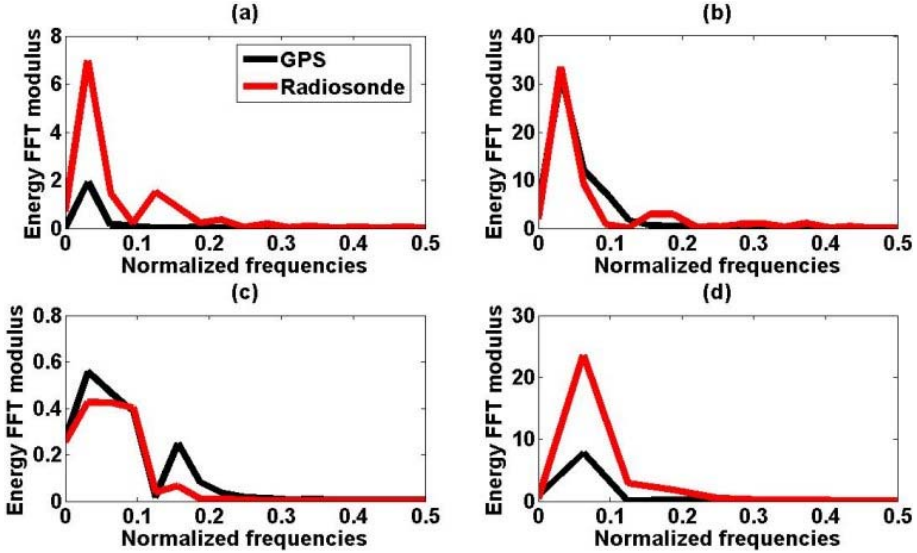

Fig. 7. Fast Fourier transform of collocated GPS RO temperature perturbations on 15 February 2008 in **(a)** the UT and **(b)** the LS above Gillot. **(c)** and **(d)** same as **(a)** and **(b)** but on 16 February 2008 above Ivato (λ_v =100 m/normalized frequency).

ACPD
13, 10757–10807, 2013

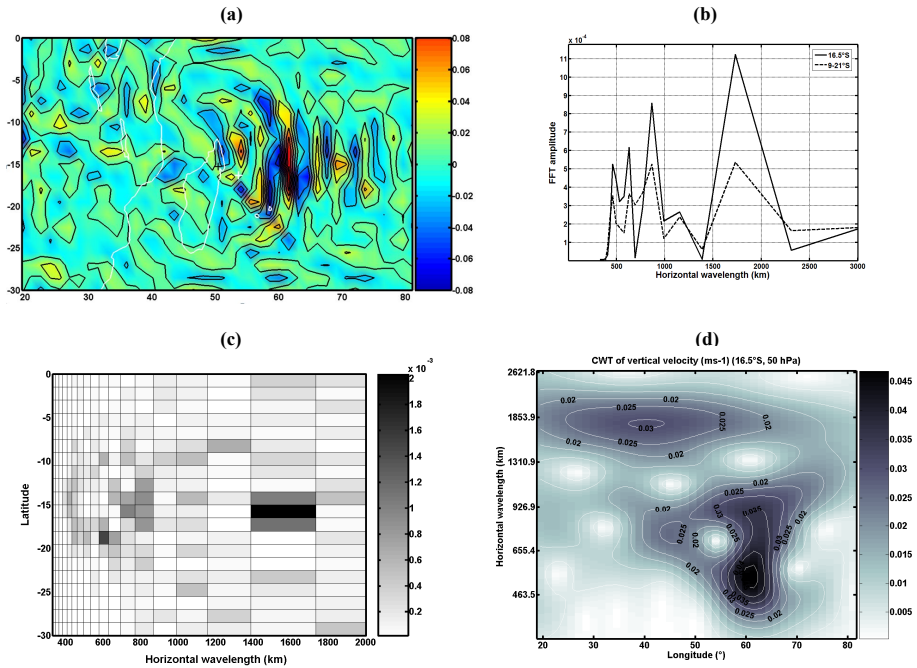

Fig. 8. (a) Vertical velocity ($m\,s^{-1}$, color) at 50 hPa derived from ECMWF analyses on 16 February 2008 (00:00 UTC). The black (white) cross locates the centre of semi-circular waves (TC Ivan). Fast Fourier Transform of vertical velocity **(b)** at latitudes of 16.5° S and 9–21° S and **(c)** as a function of latitude. **(d)** Morlet continuous wavelet transform of vertical velocity at 16.5° S.

ACPD
13, 10757–10807, 2013

Observation and a numerical study of gravity waves

F. Chane Ming et al.

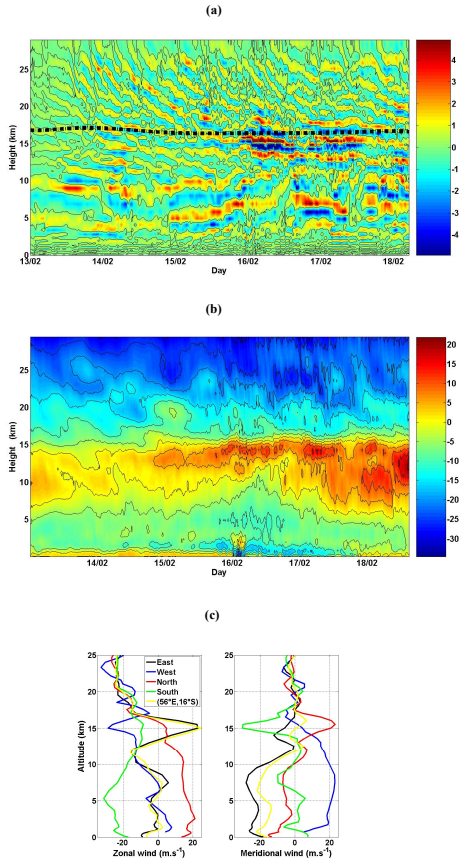

Fig. 9. (a) 10 min time series of vertical profile of meridional wind perturbations ($m s^{-1}$) at Tromelin (15.53° S, 54.31° E) and **(b)** mean zonal wind ($m s^{-1}$) at Gillot (20° 53′ S, 55° 30′ E) from 13 February (00:00 UTC) to 18 February 2008 (12:00 UTC). The bold broken line shows the tropopause height. **(c)** Vertical profiles of zonal and meridional winds at 300 km (north, east, south and west) and east at (56° E, 16° S) off the TC centre on 16 February at 06:00 UTC.

ACPD
13, 10757–10807, 2013

Observation and a numerical study of gravity waves

F. Chane Ming et al.

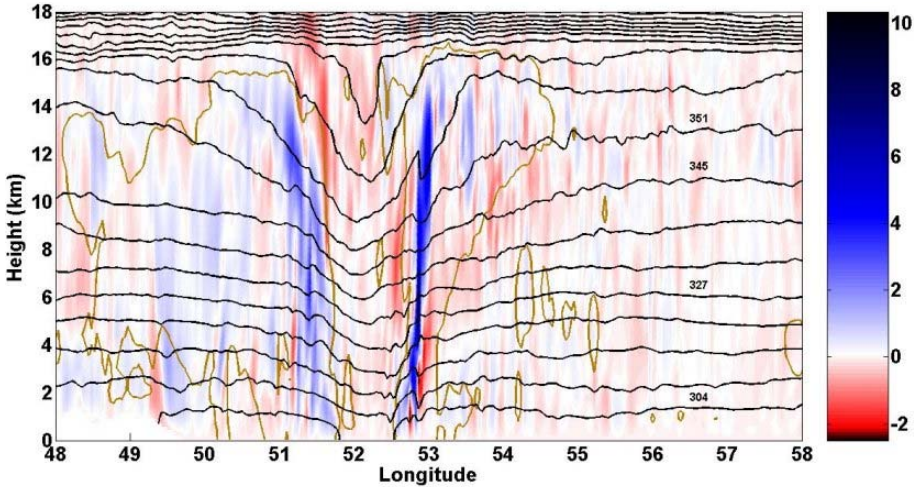

Fig. 10. Vertical cross section of vertical wind velocity ($m\,s^{-1}$) across the storm centre at 16.1° S on 16 February 2008 at 12:00 UTC. The black and brown solid lines respectively indicate iso-theta contours and the boundary of cloud, which is defined by the region where the sum of mixing ratios is $> 0.1\,g\,kg^{-1}$.

ACPD
13, 10757–10807, 2013

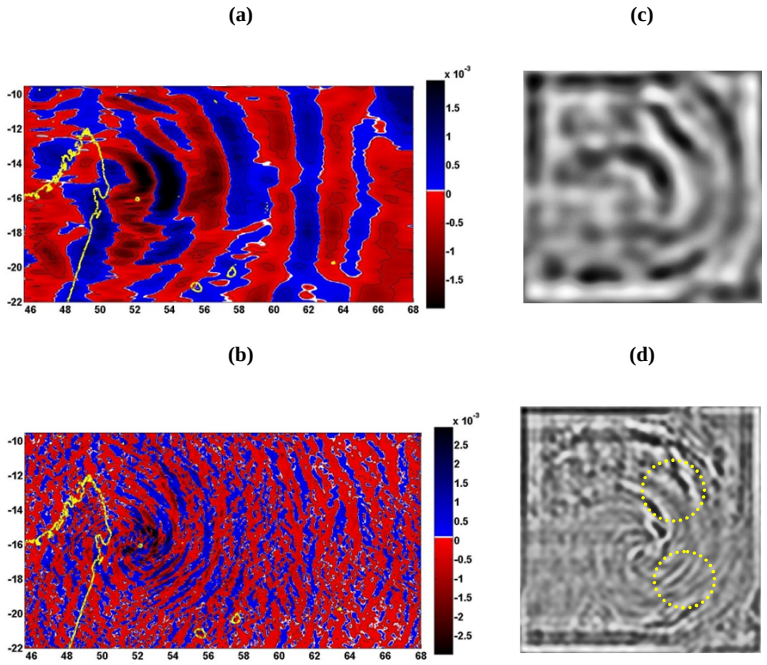

Fig. 11. Horizontal field of pressure perturbations at 20 km altitude on 16 February 2008 at 12:00 UTC for horizontal wavelengths between **(a)** 200 km and 800 km, **(b)** < 200 km. A yellow dot indicates the location of TC eye. Binary filtered images using bidimensional FFT applied on left square regions of images **(a)** and **(b)** for modes with horizontal wavelengths of **(c)** 400–600 km and **(d)** < 200 km respectively. Yellow dotted circles show the presence of GW modes in the south–east and north–east areas.

ACPD
13, 10757–10807, 2013

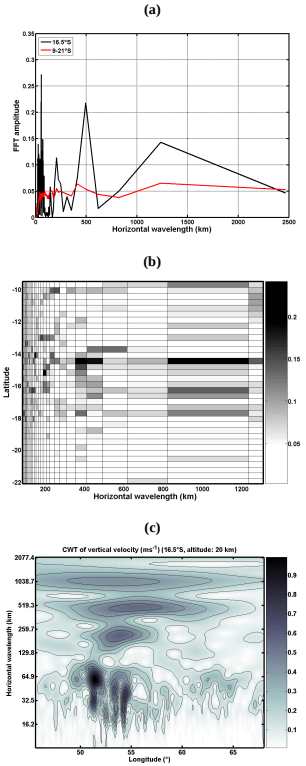

Fig. 12. Fast Fourier Transform of vertical velocity ($m\,s^{-1}$) **(a)** at latitudes of 16.5° S and 9–21° S and **(b)** as a function of latitude at the altitude of 20 km on 16 February 2008 at 12:00 UTC. **(c)** Morlet continuous wavelet transform of vertical velocity at 16.5° S.

ACPD
13, 10757–10807, 2013

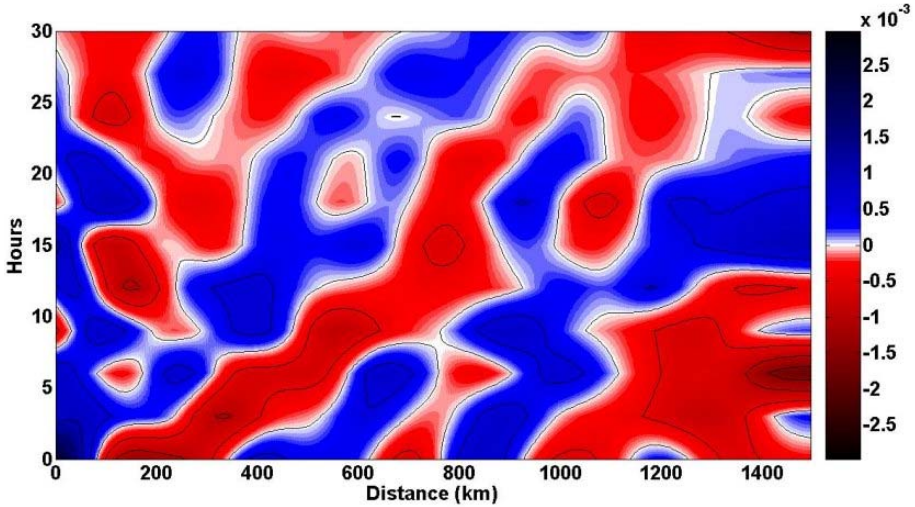

Fig. 13. Hovmoller diagram of longitudinal pressure perturbation at 16° S from 16 February 2008 at 12:00 UTC to 17 February at 18:00 UTC at 20 km.

ACPD
13, 10757–10807, 2013

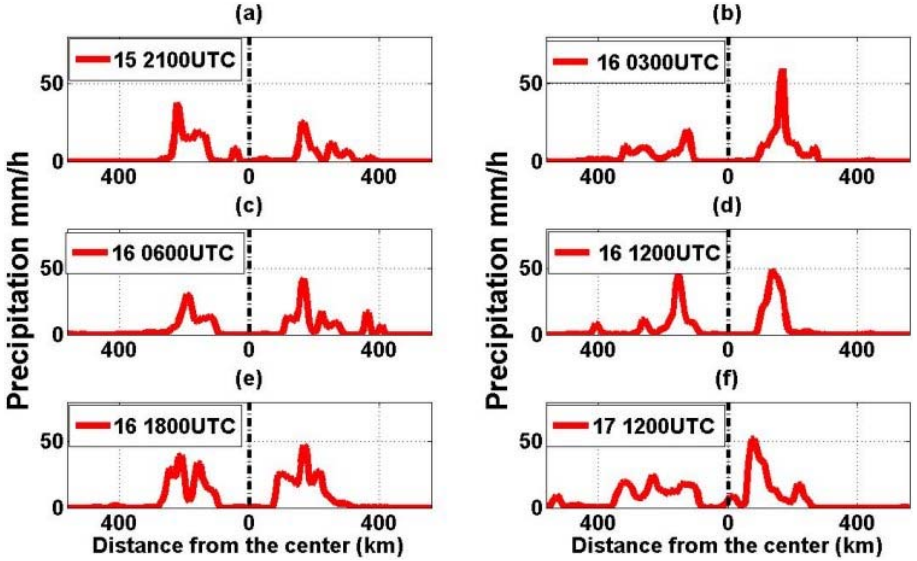

Fig. 14. Longitudinal precipitation ($mm\,h^{-1}$) cross section at a centre of TC Ivan on 15 February 2008 at 21:00 UTC **(a)**, 16 February at 03:00 UTC **(b)**, at 06:00 UTC **(c)**, at 12:00 UTC **(d)**, at 18:00 UTC **(e)**, and 17 February at 12:00 UTC **(f)**.

ACPD
13, 10757–10807, 2013

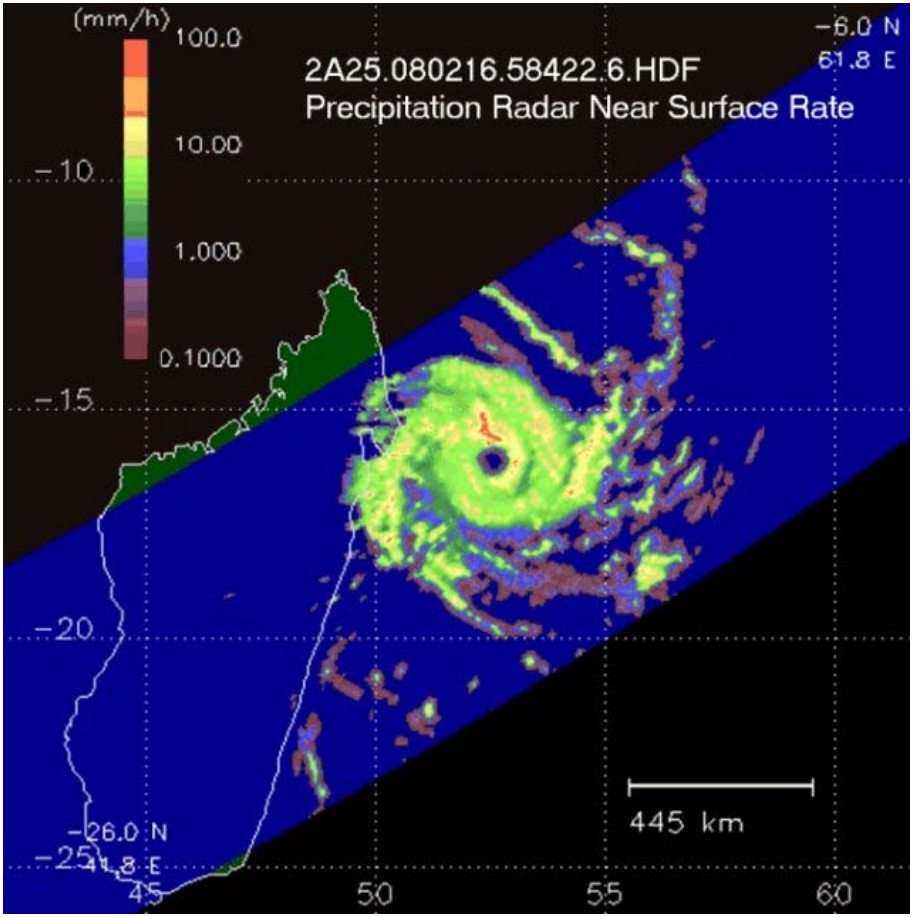

Fig. 15. TRMM Precipitation radar near surface precipitation rate from 16 February 2008 06:05:43 to 16 February 2008 07:38:06 UTC.

ACPD
13, 10757–10807, 2013

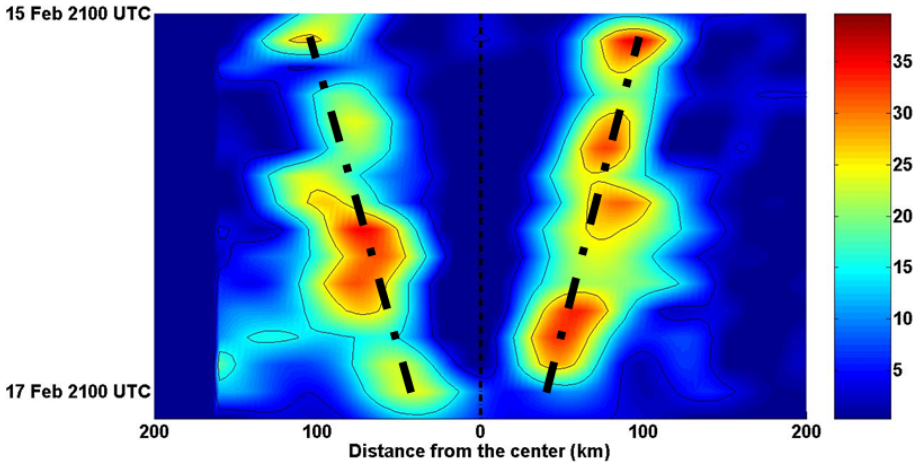

Fig. 16. Time evolution of smoothed meridional precipitation at latitude of TC centre from 15 February at 21:00 UTC to 17 February at 21:00 UTC. TC centre is used as origin for distance. Dotted broken lines indicate eye contraction.

ACPD
13, 10757–10807, 2013